

Solvent-scaling as an alternative to coarse-graining in adaptive-resolution simulations: The adaptive solvent-scaling (AdSoS) scheme

Cite as: J. Chem. Phys. 155, 094107 (2021); doi: 10.1063/5.0057384

Submitted: 20 May 2021 • Accepted: 20 July 2021 •

Published Online: 7 September 2021



View Online



Export Citation



CrossMark

Alžbeta Kubincová,  Sereina Riniker,  and Philippe H. Hünenberger^{a)} 

AFFILIATIONS

Laboratory of Physical Chemistry, Department of Chemistry and Applied Biosciences, ETH Zurich,
Vladimir Prelog-Weg 2, CH-8093 Zürich, Switzerland

^{a)}Author to whom correspondence should be addressed: phil@igc.phys.chem.ethz.ch

ABSTRACT

A new approach termed Adaptive Solvent-Scaling (AdSoS) is introduced for performing simulations of a solute embedded in a fine-grained (FG) solvent region itself surrounded by a coarse-grained (CG) solvent region, with a continuous FG \leftrightarrow CG switching of the solvent resolution across a buffer layer. Instead of relying on a distinct CG solvent model, the AdSoS scheme is based on CG models defined by a dimensional scaling of the FG solvent by a factor s , accompanied by an s -dependent modulation of the atomic masses and interaction parameters. The latter changes are designed to achieve an isomorphism between the dynamics of the FG and CG models, and to preserve the dispersive and dielectric solvation properties of the solvent with respect to a solute at FG resolution. This scaling approach offers a number of advantages compared to traditional coarse-graining: (i) the CG parameters are immediately related to those of the FG model (no need to parameterize a distinct CG model); (ii) nearly ideal mixing is expected for CG variants with similar s -values (ideal mixing holding in the limit of identical s -values); (iii) the solvent relaxation timescales should be preserved (no dynamical acceleration typical for coarse-graining); (iv) the graining level N_G (number of FG molecules represented by one CG molecule) can be chosen arbitrarily (in particular, $N_G = s^3$ is not necessarily an integer); and (v) in an adaptive-resolution scheme, this level can be varied continuously as a function of the position (without requiring a bundling mechanism), and this variation occurs at a constant number of particles per molecule (no occurrence of fractional degrees of freedom in the buffer layer). By construction, the AdSoS scheme minimizes the thermodynamic mismatch between the different regions of the adaptive-resolution system, leading to a nearly homogeneous scaled solvent density $s^3\rho$. Residual density artifacts in and at the surface of the boundary layer can easily be corrected by means of a grid-based biasing potential constructed in a preliminary pure-solvent simulation. This article introduces the AdSoS scheme and provides an initial application to pure atomic liquids (no solute) with Lennard-Jones plus Coulomb interactions in a slab geometry.

© 2021 Author(s). All article content, except where otherwise noted, is licensed under a Creative Commons Attribution (CC BY) license (<http://creativecommons.org/licenses/by/4.0/>). <https://doi.org/10.1063/5.0057384>

I. INTRODUCTION

Classical molecular dynamics (MD) simulations provide insight into the connection between microscopic interactions and macroscopic properties in the context of (bio)molecular systems, thereby explaining and complementing experimental observations. However, when carried out at fully atomistic resolution, these simulations are computationally intensive, resulting in severe limitations concerning the accessible system sizes and timescales. One

general strategy to limit the computational cost is to reduce the number of degrees of freedom involved in the calculation, i.e., to treat some of them implicitly rather than explicitly. The influence of the implicit degrees of freedom on the explicit ones is then handled by introducing corresponding mean-force (and, possibly, fluctuation) terms.

Considering solvated (macro)molecules, one may distinguish two main approaches to reduce the number of degrees of freedom: implicit-solvent and coarse-grained models. In implicit-solvent

models,^{1–6} the solvent is omitted and its influence on the solute degrees of freedom is represented by mean-force (non-polar and electrostatic) and fluctuation (stochastic and frictional) terms. In coarse-grained (CG) models,^{7–19} the resolution of the solute and/or solvent is reduced from individual atoms to beads representative of small groups of atoms, and the mean effect of the omitted intra-bead degrees of freedom is reintroduced by an appropriate parameterization of the effective potential energy function for inter-bead interactions. An early example of this approach is the use of united-atoms to represent the aliphatic CH_n group as a single interaction site.²⁰ United-atoms are often employed in models that are otherwise at fully atomistic resolution, and the word fine-grained (FG) will be used here to denote models at (united-)atom resolution.

Numerous hybrid methods combine FG and CG representations within the same calculation, attempting to strike a favorable balance between the higher accuracy of the FG resolution and the higher efficiency of the CG resolution. These so-called multi-scaling approaches^{7,8,17,21–25} can be classified into four main categories: (i) back mapping, where trajectories from CG simulations are converted to the FG level during post-processing;^{22,26–36} (ii) resolution exchange, where the entire system switches between the FG and CG representations over the course of a simulation;^{37–46} (iii) guided sampling, where coupled simulations are performed simultaneously at the FG and CG levels, the latter driving an accelerated dynamics in the former;^{47–54} and (iv) mixed or adaptive resolution, where FG and CG regions coexist spatially within the same system (references provided below).

Considering a single solute in a given solvent (e.g., hydrated macromolecule or lipid bilayer), mixed- and adaptive-resolution approaches typically aim at combining an accurate FG description in and close to the solute with a cheaper CG description of the bulk solvent. The separation between FG and CG regions involves the existence of a boundary, which may be characterized by the following features:^{55–69} (i) geometry, e.g., slab for a bilayer or spherical for a macromolecule; (ii) location, e.g., between a FG solute and a CG solvent or between a FG solute plus FG solvation layer and a CG solvent; (iii) rigidity, i.e., whether the boundary is fixed or flexible in terms of shape and position relative to the solute; (iv) thickness, i.e., whether the boundary is a dividing surface or a buffer layer; (v) permeability, i.e., whether the boundary is permeable or impermeable to the FG and CG particles and, if permeable, whether the exchange involves diffusion (FG+CG mixing) or interconversion (FG \leftrightarrow CG transformation); and (vi) possible application of a potential at this boundary, e.g., restraints to segregate the FG and CG particles, or correction potential to prevent density artifacts.

A particularly interesting combination^{22,59,61–70} relies on the use of a finite-thickness boundary (either fixed or flexible) separating a FG solute plus FG solvation layer from a CG solvent. On the one hand, compared to a direct solvation of the FG solute in the CG solvent, this combination provides a much more accurate FG treatment of the interface between the solute and its first solvation shells.^{59,63,64,71–81} On the other hand, considering that solvent–solvent interactions in the bulk are typically determinant in terms of computational costs, it is also expected to retain most of the efficiency gain associated with a CG resolution of the solvent. In practice, the computational gain will depend on the level

of graining N_G of the CG solvent model, defined as the number of FG solvent molecules mapped to a single CG molecule (typically an integer with $N_G \geq 1$). Another key advantage of this setup is that it only requires the design of a CG model for the solvent, which is generally much easier than the corresponding task for the solute. There exist two main variants of this approach concerning the treatment of the buffer layer separating FG and CG solvent regions.

In the mixed-resolution variant, the FG and CG molecules are allowed to mix in the buffer region.^{59,61–65} Spontaneous segregation may occur if the FG and CG models have poor mixing properties.⁶² Otherwise, the extent of mixing may be controlled by means of restraints relative to the solute, with attractive and/or repulsive components for the FG and CG solvent particles, respectively. In the adaptive-resolution variant,^{66–69} the FG and CG particles interconvert into each other as they go through the buffer region. When $N_G = 1$, this can be achieved by morphing, i.e., interpolating between the interaction potentials or forces of the FG and CG models using a coupling variable that varies continuously with position across the buffer layer. When $N_G > 1$, the transformation maps unequal numbers of solvent molecules and may be combined with a bundling scheme that associates clusters of nearby FG molecules to a single CG bead.^{69,70,82–85}

The most popular adaptive-resolution schemes relying on morphing across a fixed buffer layer are the Adaptive Resolution Simulation (AdResS) scheme^{86–90} and its Hamiltonian (H-AdResS)^{25,66–70,82,91–94} variant (see also Refs. 22 and 95–102 for related schemes). Here, the buffer region is defined by an internal (FG to buffer) and an external (buffer to CG) boundary, both of which are fixed in space relative to the solute. Between the two boundaries, the resolution of a solvent particle changes progressively according to a switching parameter λ that is a continuous function of position and evaluates to 1 (full FG) and to 0 (full CG) at the inner and outer boundaries, respectively. This progressive switching can be performed using two different schemes:^{25,66,89} (i) force interpolation,^{86,87,89} where the parameter λ is used to scale the forces associated with the particle at the FG (weight λ) and at the CG (weight $1 - \lambda$) resolutions, or (ii) energy interpolation,^{91–95,103} where the parameter λ is used to scale the corresponding energies instead. Using force interpolation, Newton's third law is satisfied by construction, but the weighted force does not derive from a potential, so that energy conservation may be violated. Using energy interpolation, energy conservation is satisfied by construction, but the weighted force has a component along the gradient of the switching parameter λ in space, so that Newton's third law may be violated. Irrespective of the above choices, adaptive-resolution schemes relying on a buffer layer with FG \leftrightarrow CG solvent interconversion (as well as the closely related mixed-resolution schemes) have three main shortcomings.

First, for a given choice of solvent (typically water), they rely on a unique graining level N_G that must be selected prior to the design of a model for the CG solvent. If an efficient algorithm is used for the calculation of the pairwise interactions in the MD simulation, i.e., achieving (nearly) linear scaling with the system size, the maximal achievable computational gain is then limited to N_G . Second, given the choice of a solvent and of a graining level, the CG model must be parameterized, which is a non-trivial task, or an existing model must be taken from the literature. For water, many different CG models are available,^{10,104–116} with N_G ranging from 1 to 10.

The accuracy of a given CG representation will depend in particular on how well it reproduces the pure-liquid and self-solvation properties of the solvent.^{62,75,81,117} Third, adaptive- or mixed-resolution simulations are typically affected by boundary artifacts, arising from a limited compatibility between the selected FG and CG representations, as well as from the presence of interfaces within the system. Even if a CG model has been calibrated against a given FG model, some extent of non-ideal mixing and imbalanced cross-solvation properties is unavoidable. In the case where $N_G > 1$ and the FG \leftrightarrow CG interconversion involves bundling, the system may also be affected by deficiencies inherent to bundled water models.^{118,119}

Artifacts arising from a thermodynamic mismatch between the FG and CG models can be largely remedied by applying a correcting potential accounting for the chemical-potential difference between the two models.^{88,92–94,101} Residual interfacial artifacts in the density are commonly removed via application of an *ad hoc* thermodynamic force acting in the direction of the local density gradient.^{89,90} Additionally, the insertion of solvent atoms during the FG-CG interconversion may give rise to very large forces, which need to be avoided by force capping¹²⁰ or by energy minimization.¹²¹ Finally, when $N_G > 1$, possible issues related to using a bundled water model can be alleviated by converting the bundled FG model to a supramolecular CG model across the boundary, e.g., using the SWINGER approach.^{83–85} Given these adjustments, the AdResS scheme is in principle able to combine a given FG solvent model with any CG solvent model irrespective of its thermodynamic compatibility and graining level.

This article addresses the above shortcomings in a different way, namely by introducing a simple and elegant approach to derive CG models of arbitrary graining levels directly based on a given FG solvent model. The mapping involves a scaling of the spatial dimensions by a factor s , with the FG model corresponding to $s = 1$, along with a corresponding s -dependent adjustment of the force-field parameters of the solvent molecule. For a given value of s , the CG model thus represents a “blown-up” version of the FG model, which involves the same number of interaction sites but different atomic parameters, and corresponds to a graining level $N_G = s^3$. By selecting an appropriate s -dependence of the atomic parameters, it is possible to preserve the dispersive and dielectric solvation properties with respect to a solute at FG resolution. The relaxation timescale of these properties is also unaffected, in contrast to the acceleration of the dynamics usually observed in traditional coarse-graining.^{122–124}

This scaling approach offers a number of advantages compared to traditional coarse-graining schemes: (i) the CG parameters are immediately related to those of the FG model (no need to parameterize a distinct CG model); (ii) nearly ideal mixing is expected for CG variants with similar s -values (ideal mixing holding in the limit of identical s -values); (iii) the solvent relaxation timescales should be preserved (no dynamical acceleration typical for coarse-graining); (iv) the graining level N_G can be chosen arbitrarily (in particular, $N_G = s^3$ is not necessarily an integer); and (v) in an adaptive-resolution scheme, this level can be varied continuously as a function of the position (without requiring a bundling mechanism), and this variation occurs at a constant number of particles per molecule (no occurrence of fractional degrees of freedom^{125,126} in the buffer layer).

Based on these ideas, we propose a new adaptive-resolution scheme called Adaptive Solvent-Scaling (AdSoS), where the parameter s , which governs the scaling of the solvent, varies as a function of the position of a solvent molecule in space. Starting from $s = 1$ in the FG region close to the solute, the value of s is progressively increased across a buffer layer to reach a value s_{max} , which is then kept constant in the long-range CG region. Here, an initial application of the AdSoS approach is presented, considering a simple monoatomic solvent with Lennard-Jones¹²⁷ plus Coulomb¹²⁸ interactions in a slab geometry. Extension to water, spherical geometry, and systems involving solutes will be presented in a subsequent article.

II. THEORY

A. Intuitive considerations

The goal of this section is to provide an intuitive overview of the solvent-scaling approach, defining the FG-to-CG mapping in the AdSoS scheme. The concepts presented here will be formalized in Secs. II B–II E.

The dynamics of a physical system is described by quantities with units, which can be expressed as combinations of fundamental units of length, mass, time, and charge (e.g., meter, kilogram, second, and Coulomb in the SI system). However, the equations governing the system dynamics are independent of a specific choice for the fundamental units. An interesting corollary to this principle is the following. If one defines a scaling of the fundamental units and absorbs the corresponding scaling factors into the physical quantities, one obtains a scaled system that still obeys the same equations of motion as the original one. In other words, such a scaling represents a form of physical isomorphism in terms of the system dynamics.

The transformation considered here is defined by a unitless scaling factor s , initially assumed constant, i.e., independent of space and time. This parameter controls the following scaling of the fundamental units

$$\{\tilde{r}, \tilde{m}, \tilde{t}, \tilde{q}\} = \{sr^*, s^{-2}m^*, t^*, s^{1/2}q^*\}, \quad (1)$$

where r , m , t , and q stand for the length, mass, time, and charge, respectively. The quantities with a star correspond to the original physical system, and those with a tilde correspond to the scaled system. It will be shown in Secs. II B–II E that the above scaling of the fundamental units: (i) scales the coordinates, velocities, and accelerations by s ; (ii) scales the forces by s^{-1} ; (iii) leaves time and energy invariant; and (iv) leaves the dynamics (e.g., the classical Hamiltonian equations of motion) unaltered.

As an illustrative example, consider a system consisting of an apple of 1 kg at a height of 5 m with a downward velocity of 1 m s⁻¹ and subject to a gravitational acceleration of 10 m s⁻² giving a force of 10 N. The corresponding scaled system with $s = 2$ will consist of a “scaled” apple of 0.25 kg at 10 m from the ground with a downward velocity of 2 m s⁻¹ and subject to a gravitational acceleration of 20 m s⁻² giving a force of 5 N. The kinetic and potential energies of the two systems are the same (0.5 and 50 J, respectively). Applying Newton’s second law to propagate the dynamics of both systems in time will produce isomorphic trajectories, i.e., trajectories in which the configurations remain scaled variants of each other at all times. The coordinates and velocities for the scaled system are amplified by s , while the energies of the two systems remain identical.

Considering a classical molecular system where the interatomic interactions include a Lennard-Jones and a Coulomb component, the scaling of various physical quantities (atomic interaction parameters, configurational variables, and thermodynamic observables) associated with the scaling of Eq. (1) is summarized in Table I. Mathematically, one has to impose $s > 0$ because the s -dependent scalings of the various physical quantities (Table I) involve fractional (undefined for $s \leq 0$) as well as negative (undefined for $s = 0$) powers.

Irrespective of the choice of s , the microcanonical (NVE) trajectory of a scaled system will remain isomorphic to that of the original system, provided that an appropriate scaling of the initial configuration (coordinates and velocities amplified by s , volume multiplied by s^3 , and identical energy), masses (scaled by s^{-2}), and interaction parameters (Lennard-Jones c_6 and c_{12} square-root coefficients amplified by s^3 and s^6 , respectively, and charges multiplied by $s^{1/2}$) has been applied. The same observation applies to the canonical situation (NVT, thermostated dynamics), considering that the temperature, which is proportional to the kinetic energy, is unaffected by the scaling. Extension to isothermal-isobaric conditions (NPT, thermo- and barostated dynamics) is also straightforward, albeit with an important proviso. Since the pressure is amplified by s^{-3} upon scaling, the corresponding reference pressure must be adjusted accordingly to achieve isomorphic trajectories.

In the special case where the system is a pure solvent described by a selected FG model at $s = 1$ (unscaled system), a scaled model with $s > 1$ is expected to provide a reasonable CG description of this liquid for three reasons. First, comparing volume elements ΔV of the FG solvent and of its scaled variant, as illustrated in Fig. 1 for a monoatomic solvent, one observes that the number of particles inside ΔV is reduced by a factor of s^{-3} upon scaling. This results in an effective graining level $N_G = s^3$, which is not necessarily an integer. Second, the above isomorphism implies that the relaxation

TABLE I. Dependence of various physical quantities on the scaling factor s considering a classical molecular system subject to Lennard-Jones and Coulomb interactions. The scaling of the quantities is defined by $\tilde{Q} = f(s) Q^*$, where Q^* is the quantity in the original physical system and \tilde{Q} is the corresponding quantity in the scaled system. The atomic parameters considered are the mass (m), the charge (q), and the Lennard-Jones parameters (c_6 and c_{12}). The latter parameters correspond to single-atom root-mean-square dispersion and repulsion coefficients, respectively. Their products determine the magnitude of the corresponding interactions for two given atoms (geometric-mean combination rule). The configurational variables considered are the time (t), coordinate (r), volume (V), velocity (v), momentum (p), and force (F). The thermodynamic observables considered are the Hamiltonian (\mathcal{H}), kinetic energy (\mathcal{K}), potential energy (\mathcal{U}), virial (\mathcal{W}), temperature (T), pressure (P), number density (ρ), isothermal compressibility (κ), and relative dielectric permittivity (ϵ).

$f(s)$	Parameter	Configuration	Observable
s^{-3}			ρ, P
s^{-2}	m		
s^{-1}		F, p	
1		t	$\mathcal{H}, \mathcal{U}, \mathcal{K}, \mathcal{W}, T, \epsilon$
$s^{1/2}$	q		
s		r, v	
s^3	c_6	V	
s^6	c_{12}		κ

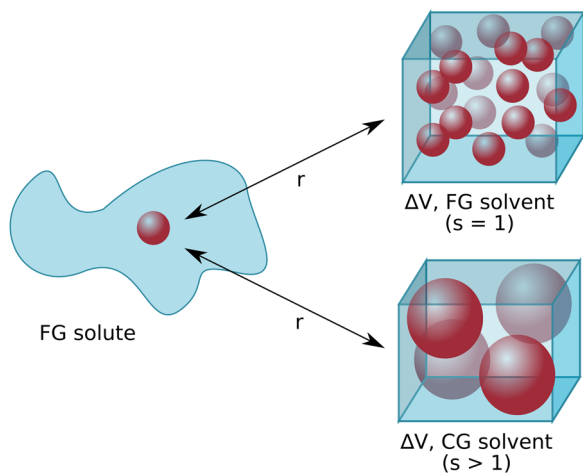


FIG. 1. Schematic illustration of a solute at FG resolution interacting with volume elements of the FG and scaled CG models. A FG atom in the solute has the same dispersive interaction with a solvent volume element ΔV at a given distance r irrespective of whether it is filled with FG solvent or with a scaled CG version of this solvent. The same holds for the electrostatic interaction energy of a dipolar solvent with the FG solute, as the dielectric permittivity is unaffected by the scaling.

properties (timescales) should be identical for the two volume elements. Third, most importantly, the solvation properties of the two volume elements with respect to a solute at FG resolution are expected to be nearly identical. The reasoning underlying this last statement is also illustrated in Fig. 1.

Concerning the Lennard-Jones interactions, consider a solute FG atom interacting with the volume element ΔV of scaled CG solvent. For the dispersion component, the c_6 single-atom coefficient of the solvent is scaled by s^3 , while the number of solvent molecules in ΔV is scaled by s^{-3} . The two effects compensate each other, i.e., the volumetric dispersive solvation properties of the solvent are the same at the FG and CG levels. This is not the case for the repulsion component, which increases as s^3 (factor s^6 for the c_{12} single-atom coefficient of the solvent times factor s^{-3} for the solvent number density). However, the magnitude of this repulsive term in r^{-12} decreases rapidly with the distance from the solute, i.e., this effect is expected to become negligible if the CG model is employed sufficiently far from the solute (as should be the case in the AdSoS scheme). Concerning the Coulomb interactions and restricting the discussion to a neutral solute in a dipolar solvent, the relevant factor is not the scaling of the solvent charges ($s^{1/2}$) and number density (s^{-3}), but that of the relative dielectric permittivity. Since the permittivity is a unitless intensive quantity, it is not affected by the scaling. This can also be seen from the connection between ϵ and $\langle M^2 \rangle/V$, which is invariant upon scaling, for a volume V with dipole-moment fluctuations $\langle M^2 \rangle$. Consequently, the dipolar solvation of the solute is also the same at the FG and CG levels. The dielectric (Debye) relaxation time of the solvent is also preserved by the scaling. Note that although the above arguments hold for any s -value in the mathematically allowed range ($s > 0$), it also makes sense computationally to further restrict this range to $s \geq 1$. Lower s -values would define scaled models that are downsized relative to the FG model ($s = 1$), i.e., more expensive to simulate compared to this model, which is inconsistent with the purpose of coarse-graining.

Sections II B–II H provide a more formal description of the solvent-scaling approach and of the adaptive-resolution scheme inspired by the above considerations. It is restricted to the following situation: (i) an atomic liquid with pairwise Lennard-Jones¹²⁷ and Coulomb¹²⁸ interactions, the former with a geometric-mean combination rule;^{129,130} (ii) an adaptive-resolution setup involving the pure solvent in a slab geometry (no solute). A subsequent article will describe the extension of the scheme to a molecular solvent (water), a system in spherical geometry, and situations involving a solute.

B. Reference system

Consider a reference system of N atoms at FG resolution, the associated quantities being labeled with a star superscript. The system is characterized by the $3N$ -dimensional Cartesian coordinate and momentum vectors \mathbf{r}^* and \mathbf{p}^* , along with a Hamiltonian

$$\mathcal{H}^*(\mathbf{r}^*, \mathbf{p}^*) = \mathcal{K}^*(\mathbf{p}^*) + \mathcal{U}^*(\mathbf{r}^*), \quad (2)$$

where \mathcal{U}^* and \mathcal{K}^* are the kinetic and potential energies, respectively. The dynamics of the system obeys the Hamiltonian equations of motion,

$$\frac{d\mathbf{p}^*}{dt} = -\frac{\partial \mathcal{H}^*(\mathbf{r}^*, \mathbf{p}^*)}{\partial \mathbf{r}^*} \quad \text{and} \quad \frac{d\mathbf{r}^*}{dt} = \frac{\partial \mathcal{H}^*(\mathbf{r}^*, \mathbf{p}^*)}{\partial \mathbf{p}^*}, \quad (3)$$

where t stands for time.

In the specific case of an atomic liquid with Lennard-Jones plus Coulomb interactions, the terms of Eq. (2) take the form

$$\mathcal{K}^*(\mathbf{p}^*) = \sum_i^N \frac{\mathbf{p}_i^{*2}}{2m_i^*} \quad (4)$$

and

$$\begin{aligned} \mathcal{U}^*(\mathbf{r}^*) = & -\sum_i^N \sum_{j>i}^N c_{6,i}^* c_{6,j}^* r_{ij}^{*-6} + \sum_i^N \sum_{j>i}^N c_{12,i}^* c_{12,j}^* r_{ij}^{*-12} \\ & + \frac{1}{4\pi\epsilon_0} \sum_i^N \sum_{j>i}^N q_i^* q_j^* r_{ij}^{*-1}, \end{aligned} \quad (5)$$

where $r_{ij}^* = |\mathbf{r}_i^* - \mathbf{r}_j^*|$ is the distance between atoms i and j , and ϵ_0 is the permittivity of vacuum. The force-field parameters involved in these expressions are the mass m_i^* and charge q_i^* of an atom i , along with its square-root Lennard-Jones coefficients $c_{6,i}^*$ (dispersion) and $c_{12,i}^*$ (repulsion).

The systems considered in practice are subject to periodic boundary conditions based on a computational box of fixed volume V^* , and are possibly coupled to a thermostat at a reference temperature T . To keep the equations as simple as possible, the corresponding modifications of Eqs. (2)–(5) are not introduced explicitly. Note also that the star superscript is omitted from the quantities N , T , and t for simplicity, as they will not be affected by the scaling (i.e., $t^* = t$, $N^* = N$, and $T^* = T$).

C. System scaling in terms of configuration

Next, consider a scaled system where a fixed parameter s is introduced to alter the coordinates and momenta of the reference system. In the following, a tilde overscript will be used to indicate

quantities with an explicit functional dependence on the reference-system quantity (star superscript) and on the scaling factor (s). The scaling is defined by

$$\tilde{\mathbf{r}} \doteq \tilde{\mathbf{r}}(\mathbf{r}^*, s) = s\mathbf{r}^*, \quad \tilde{\mathbf{p}} \doteq \tilde{\mathbf{p}}(\mathbf{p}^*, s) = s^{-1}\mathbf{p}^*,$$

and

$$\tilde{V} \doteq \tilde{V}(V^*, s) = s^3 V^*. \quad (6)$$

As stated earlier, the quantities N , T , and t are not altered (i.e., $\tilde{t} = t^* = t$, $\tilde{N} = N^* = N$, and $\tilde{T} = T^* = T$).

For any fixed choice of s , a scaled trajectory of the reference system is defined as the trajectory generated by propagating the reference system (\mathbf{r}^* and \mathbf{p}^*) as a function of t for given V^* and T) using Eq. (3) with the Hamiltonian $\mathcal{H}^*(\mathbf{r}^*, \mathbf{p}^*)$ of Eq. (2), followed by a scaling of the successive configurations using Eq. (6).

D. Trajectory isomorphism

At this point, assume that one can engineer a Hamiltonian \mathcal{H} for which the energetic quantities are invariant upon scaling, i.e., satisfying

$$\mathcal{H}(\tilde{\mathbf{r}}, \tilde{\mathbf{p}}, s) = \mathcal{K}(\tilde{\mathbf{p}}, s) + \mathcal{U}(\tilde{\mathbf{r}}, s) = \mathcal{H}^*(\mathbf{r}^*, \mathbf{p}^*)$$

with

$$\mathcal{K}(\tilde{\mathbf{p}}, s) = \mathcal{K}^*(\mathbf{p}^*) \quad \text{and} \quad \mathcal{U}(\tilde{\mathbf{r}}, s) = \mathcal{U}^*(\mathbf{r}^*). \quad (7)$$

In the specific case of the atomic liquid with Lennard-Jones plus Coulomb interactions, the terms of this Hamiltonian read

$$\mathcal{K}(\tilde{\mathbf{p}}, s) = \sum_i^N \frac{s^2 \tilde{\mathbf{p}}_i^2}{2m_i^*} \quad (8)$$

and

$$\begin{aligned} \mathcal{U}(\tilde{\mathbf{r}}, s) = & -\sum_i^N \sum_{j>i}^N c_{6,i}^* c_{6,j}^* s^6 \tilde{r}_{ij}^{-6} + \sum_i^N \sum_{j>i}^N c_{12,i}^* c_{12,j}^* s^{12} \tilde{r}_{ij}^{-12} \\ & + \frac{1}{4\pi\epsilon_0} \sum_i^N \sum_{j>i}^N q_i^* q_j^* s \tilde{r}_{ij}^{-1}. \end{aligned} \quad (9)$$

The Hamiltonian \mathcal{H} depends on s through its three variables, and the corresponding total derivative must be zero due to invariance upon scaling [Eq. (7)], i.e.,

$$\frac{d\mathcal{H}(\tilde{\mathbf{r}}, \tilde{\mathbf{p}}, s)}{ds} = \left(\frac{\partial \mathcal{H}}{\partial \tilde{\mathbf{r}}} \right)_{\tilde{\mathbf{p}}, s} \left(\frac{\partial \tilde{\mathbf{r}}}{\partial s} \right)_{\mathbf{r}^*} + \left(\frac{\partial \mathcal{H}}{\partial \tilde{\mathbf{p}}} \right)_{\tilde{\mathbf{r}}, s} \left(\frac{\partial \tilde{\mathbf{p}}}{\partial s} \right)_{\mathbf{p}^*} + \left(\frac{\partial \mathcal{H}}{\partial s} \right)_{\tilde{\mathbf{r}}, \tilde{\mathbf{p}}} = 0. \quad (10)$$

As shown explicitly in Appendix A for the specific case of Eqs. (8) and (9), the three terms can be identified with important system quantities, namely,

$$\begin{aligned} \left(\frac{\partial \mathcal{H}}{\partial \tilde{\mathbf{r}}} \right)_{\tilde{\mathbf{p}}, s} \left(\frac{\partial \tilde{\mathbf{r}}}{\partial s} \right)_{\mathbf{r}^*} &= 2s^{-1} \mathcal{W}(\tilde{\mathbf{r}}, s), \\ \left(\frac{\partial \mathcal{H}}{\partial \tilde{\mathbf{p}}} \right)_{\tilde{\mathbf{r}}, s} \left(\frac{\partial \tilde{\mathbf{p}}}{\partial s} \right)_{\mathbf{p}^*} &= -2s^{-1} \mathcal{K}(\tilde{\mathbf{p}}, s), \end{aligned} \quad (11)$$

and

$$\left(\frac{\partial \mathcal{H}}{\partial s} \right)_{\tilde{\mathbf{r}}, \tilde{\mathbf{p}}} = 3s^{-1} \tilde{V} \mathcal{P}(\tilde{\mathbf{r}}, \tilde{\mathbf{p}}, s), \quad (12)$$

where \mathcal{K} is the kinetic energy, \mathcal{W} is the virial, and \mathcal{P} is the pressure. These three quantities are related by the equation¹³¹

$$\mathcal{P} = \frac{2(\mathcal{K} - \mathcal{W})}{3\tilde{V}}, \quad (13)$$

which is consistent with the vanishing total derivative in Eq. (10).

Combining the Hamiltonian equations of motion for the reference system in Eq. (3) with the scaling definitions of Eq. (6) and the requirements of Eq. (7), one obtains

$$\begin{aligned} \frac{d\tilde{\mathbf{p}}}{dt} &= s^{-1} \frac{d\mathbf{p}^*}{dt} = -s^{-1} \frac{\partial \mathcal{H}(\mathbf{r}^*, \mathbf{p}^*)}{\partial \mathbf{r}^*} \\ &= -\frac{\partial \mathcal{H}(\mathbf{r}^*, \mathbf{p}^*)}{\partial (s\mathbf{r}^*)} = -\frac{\partial \mathcal{H}(\tilde{\mathbf{r}}, \tilde{\mathbf{p}}, s)}{\partial \tilde{\mathbf{r}}} \end{aligned}$$

and

$$\begin{aligned} \frac{d\tilde{\mathbf{r}}}{dt} &= s \frac{d\mathbf{r}^*}{dt} = s \frac{\partial \mathcal{H}(\mathbf{r}^*, \mathbf{p}^*)}{\partial \mathbf{p}^*} \\ &= \frac{\partial \mathcal{H}(\mathbf{r}^*, \mathbf{p}^*)}{\partial (s^{-1}\mathbf{p}^*)} = \frac{\partial \mathcal{H}(\tilde{\mathbf{r}}, \tilde{\mathbf{p}}, s)}{\partial \tilde{\mathbf{p}}} \end{aligned} \quad (14)$$

Thus, the scaled system also obeys Hamiltonian equations of motion. The same applies for modified equations involving periodic boundary conditions [with the scaled volume \tilde{V} of Eq. (6)] and thermostating (with an unaltered temperature T).

This observation suggests that one may consider the coordinates and momenta of the scaled system as variables on their own right, instead of functions relating them to the reference system. This choice will be indicated in the following by plain symbols (i.e., dropping the tilde overscript). In this perspective, Eq. (14) is rewritten as

$$\frac{d\mathbf{p}}{dt} = -\frac{\partial \mathcal{H}(\mathbf{r}, \mathbf{p}, s)}{\partial \mathbf{r}}$$

and

$$\frac{d\mathbf{r}}{dt} = \frac{\partial \mathcal{H}(\mathbf{r}, \mathbf{p}, s)}{\partial \mathbf{p}}. \quad (15)$$

For any fixed choice of s , a trajectory of the scaled system is defined as the trajectory generated by propagating the scaled system (\mathbf{r} and \mathbf{p} as a function of t for given V and T) using Eq. (15) with the Hamiltonian $\mathcal{H}(\mathbf{r}, \mathbf{p}, s)$ satisfying Eq. (7). A scaled trajectory of the reference system [$s\mathbf{r}^*(t), s^{-1}\mathbf{p}^*(t)$] and a trajectory of the scaled system [$\mathbf{r}(t), \mathbf{p}(t)$] are then rigorously identical owing to Eq. (14), provided that their initial configurations are appropriately related by the scaling of Eq. (6). This property is referred to here as an isomorphism between the dynamics of the reference and the scaled systems.

E. System scaling in terms of force-field parameters

From this point onward, only the latter perspective of the scaled system will be retained. In this perspective, the scaling is viewed as an explicit s -dependence of the Hamiltonian $\mathcal{H}(\mathbf{r}, \mathbf{p}, s)$ without any implicit dependence through \mathbf{r} and \mathbf{p} , which are configurational variables of the scaled system on their own right. In the specific case of the atomic liquid with Lennard-Jones plus Coulomb interactions, it is convenient to introduce scaled force-field parameters,

$$\begin{aligned} \tilde{m} &\doteq \tilde{m}(m^*, s) = s^{-2}m^*, \quad \tilde{c}_6 \doteq \tilde{c}_6(c_6^*, s) = s^3c_6^*, \\ \tilde{c}_{12} &\doteq \tilde{c}_{12}(c_{12}^*, s) = s^6c_{12}^*, \quad \text{and} \quad \tilde{q} \doteq \tilde{q}(q^*, s) = s^{1/2}q^*. \end{aligned} \quad (16)$$

Inserting these definitions, the Hamiltonian terms of Eqs. (8) and (9) become

$$\mathcal{K}(\mathbf{p}, s) = \sum_i^N \frac{\mathbf{p}_i^2}{2\tilde{m}_i} \quad (17)$$

and

$$\begin{aligned} \mathcal{U}(\mathbf{r}, s) &= -\sum_i^N \sum_{j>i}^N \tilde{c}_{6,i} \tilde{c}_{6,j} r_{ij}^{-6} + \sum_i^N \sum_{j>i}^N \tilde{c}_{12,i} \tilde{c}_{12,j} r_{ij}^{-12} + \frac{1}{4\pi\varepsilon_0} \sum_i^N \sum_{j>i}^N \tilde{q}_i \tilde{q}_j r_{ij}^{-1}. \end{aligned} \quad (18)$$

Note the strong analogy between these equations and the corresponding expressions of Eqs. (4) and (5) for the reference system, which is clearly advantageous in terms of computational implementation.

A consequence of adopting the perspective of the scaled system is that the derivative of the Hamiltonian with respect to s is now a partial derivative that no longer vanishes. Only the third term in Eq. (10) is retained, i.e., that of Eq. (12), leading to

$$\frac{d\mathcal{H}(\mathbf{r}, \mathbf{p}, s)}{ds} = \left(\frac{\partial \mathcal{H}(\mathbf{r}, \mathbf{p}, s)}{\partial s} \right)_{\mathbf{r}, \mathbf{p}} = 3s^{-1}V\mathcal{P}(\mathbf{r}, \mathbf{p}, s). \quad (19)$$

Table I provides an overview of the scalings of various physical quantities (atomic interaction parameters, configurational variables, and thermodynamic observables). Note that a scaling by $s > 1$ increases the particle velocities in proportion to their coordinates (factor s for both) but decreases the particle momenta (factor s^{-1}) because the masses are simultaneously reduced (factor s^{-2}). Note also that if cutoff truncation is applied to the pairwise interactions, the isomorphism can be preserved if the cutoff distance is scaled as well, i.e.,

$$\tilde{R}_c \doteq R_c(R_c^*, s) = sR_c^*. \quad (20)$$

Of particular importance is the observation that, unlike all the energetic quantities as well as the temperature, the number density ρ , the pressure P , and the compressibility κ are not invariant upon scaling. Considering the scaling of the volume (s^3), the fact that the pressure–volume product is an energetic quantity (no scaling), and that κ has units of an inverse pressure, one has

$$\rho(s) = s^{-3}\rho^*, \quad (21)$$

$$P(s) = s^{-3}P^*, \quad (22)$$

and

$$\kappa(s) = s^3\kappa^*. \quad (23)$$

Owing to Eq. (22), the pressure under NVT conditions depends on s . Accordingly, the trajectory isomorphism upon scaling can only be preserved in the NPT ensemble if the reference pressure P_{ref} of the barostat is adjusted to the scaling factor as $s^{-3}P_{\text{ref}}^*$. However, if the scaled model is to be used as a CG representation of the solvent at the same reference pressure $P_{\text{ref}} = P^*$ as would be appropriate for the FG model, the isomorphism breaks down. In particular, the pressure increase from $s^{-3}P^*$ to P^* is expected to cause an increase in the density ρ of the system from $s^{-3}\rho^*$ [Eq. (21)] to a larger value ρ_{NPT} .

Using a first-order approximation for the density increase resulting from this pressure change leads to

$$\rho_{\text{NPT}}(s) = \frac{s^{-3}\rho^*}{1 - \kappa^*P^*(s^3 - 1)}. \quad (24)$$

The s -dependence of the s -corrected density $s^3\rho_{\text{NPT}}$ under NPT conditions at fixed (e.g., atmospheric) pressure P_{ref} may seem to represent a major drawback of CG models constructed by scaling of a given FG model, as it suggests that the liquid (and solvation) properties of the CG model will progressively deviate from those of the FG model upon increasing s . However, as discussed at the end of Sec. II F, this does not represent an issue within an adaptive-resolution scheme that can accommodate pressure inhomogeneities in such a way that a volume element of CG solvent at scaling s is in equilibrium at the pressure $s^{-3}P^*$ leading to the appropriate s -corrected density $s^{-3}\rho^*$.

F. Adaptive resolution with solvent-scaling (AdSoS scheme)

Owing to the isomorphism between the reference and the scaled solvent, and to the equivalence in their dispersive and dielectric solvation properties, the scaled solvent is an excellent candidate for the CG representation of a given FG solvent in an adaptive-resolution setup. In this case, the fixed scaling parameter s must be generalized to a function $s(\mathbf{r})$ that depends on the position of the solvent molecule.

The discussion is restricted here to a pure atomic liquid in slab geometry, as illustrated in Fig. 2. The FG compartment, which could later encompass a planar solute (e.g., membrane), is associated with a uniform scaling factor $s = 1$ corresponding to the reference FG model. The CG compartment, which is meant to account for the long-range solvation of the solute at reduced computational cost, is associated with a uniform scaling factor $s = s_{\text{max}}$, which can be chosen arbitrarily. Between the FG and the CG regions, two compartments with an s -gradient (SG) allow for a progressive switching

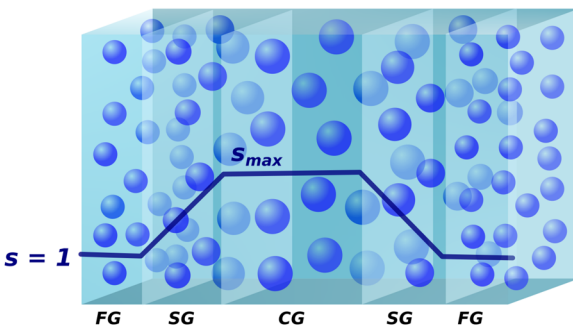


FIG. 2. The Adaptive Solvent-Scaling (AdSoS) scheme applied to a pure atomic liquid in slab geometry. The computational box is periodic along the three directions and filled with solvent atoms at different levels of scaling. The scaling parameter s affecting an atom depends on its position along the z -direction via a function $s(z)$. This function defines a fine-grained (FG) region ($s = 1$) and a coarse-grained (CG) region ($s = s_{\text{max}}$), separated by two transition regions featuring s -gradients (SGs). The FG compartment could encompass a planar solute, and the CG compartment is meant to account for the long-range solvation of this solute at reduced computational cost.

of s between 1 and s_{max} and between s_{max} and 1. The progressive evolution of the s -value along the z -direction of the box is defined by a continuous function $s(z)$. The volume of the box, the sizes of the four compartments, and the function $s(z)$ are all kept fixed during the simulation.

Because the system now involves interactions between atoms at different local s -values, an exact isomorphism to some reference system can no longer be defined, and *ad hoc* choices must be made to preserve a qualitative similarity with the homogeneous-scaling situation. The Hamiltonian retained for the AdSoS scheme reads

$$\mathcal{H}(\mathbf{r}, \mathbf{p}) = -\sum_i^N \sum_{j>i}^N s_i^3 s_j^3 c_{6,i}^* c_{6,j}^* r_{ij}^{-6} + \sum_i^N \sum_{j>i}^N s_i^6 s_j^6 c_{12,i}^* c_{12,j}^* r_{ij}^{-12} + \frac{1}{4\pi\epsilon_0} \sum_i^N \sum_{j>i}^N s_i^{1/2} s_j^{1/2} q_i^* q_j^* r_{ij}^{-1} + \sum_i^N \frac{\mathbf{p}_i^2}{2s_i^{-2} m_i^*}, \quad (25)$$

where $s_i \doteq s(\mathbf{r}_i)$ and $s_j \doteq s(\mathbf{r}_j)$. Here, an *ad hoc* choice was made to scale the interaction between atoms i and j according to a pairwise scaling factor s_{ij} that is given by the geometric mean of s_i and s_j . This choice leads to simple equations and produces the correct result when $s_i = s_j$ (e.g., when both atoms are within the FG or within the CG region). Otherwise, it provides a reasonable (though not unique) combination.

The negative derivative of the Hamiltonian of Eq. (25) with respect to the position of an atom represents the force on this atom,

$$\mathbf{F}_i = -\frac{d\mathcal{H}}{d\mathbf{r}_i} = -\left(\frac{\partial\mathcal{H}}{\partial\mathbf{r}_i}\right)_{s_i} - \left(\frac{\partial\mathcal{H}}{\partial s_i}\right)_{\mathbf{r}_i} \frac{ds_i}{d\mathbf{r}_i}. \quad (26)$$

In the context of the atomic liquid with Lennard-Jones plus Coulomb interactions, this reads

$$\mathbf{F}_i = \sum_{j \neq i} \left(-6\tilde{c}_{6,i}\tilde{c}_{6,j}r_{ij}^{-8} + 12\tilde{c}_{12,i}\tilde{c}_{12,j}r_{ij}^{-14} + \frac{\tilde{q}_i\tilde{q}_j}{4\pi\epsilon_0}r_{ij}^{-3} \right) \mathbf{r}_{ij} + \sum_{j \neq i} \left(-3\tilde{c}_{6,i}\tilde{c}_{6,j}r_{ij}^{-6} + 6\tilde{c}_{12,i}\tilde{c}_{12,j}r_{ij}^{-12} - \frac{1}{2}\frac{\tilde{q}_i\tilde{q}_j}{4\pi\epsilon_0}r_{ij}^{-1} - \frac{\mathbf{p}_i^2}{2s_i^{-2}m_i^*} \right) s_i^{-1} \frac{\partial s_i}{\partial \mathbf{r}_i}, \quad (27)$$

where $\mathbf{r}_{ij} = \mathbf{r}_i - \mathbf{r}_j$ and the scaled atomic parameters (tilde overline) are defined according to Eq. (16). The first term in the above equations represents the physical pairwise force acting along the interatomic vector. The second term represents a so-called drift force,^{67,91,132,133} which is only present in regions where s varies, and acts along the corresponding s -gradient.

The inclusion of the drift force in the dynamics of the adaptive-resolution system is essential to prevent the occurrence of density artifacts. This can be understood intuitively by considering successive slabs of widths Δz (identical volumes ΔV) along the z -axis of the box as a series of isothermal-isobaric systems. These slabs share the same temperature T , and the corresponding numbers of particles and pressures follow from Eqs. (21) and (22), namely, $\Delta N(z) = \rho(z)\Delta V$ with $\rho(z) = s^{-3}(z)\rho^*$ and $P(z) = s^{-3}(z)P^*$. Assuming a sufficient number of particles ΔN in each slab, the chemical potential is equal to the Gibbs free energy G divided by ΔN , and its total derivative with respect to s reads

$$\frac{d\mu(P, T, s)}{ds} = \frac{1}{\Delta N} \left[\left(\frac{\partial G}{\partial s} \right)_{P,T} + \left(\frac{\partial G}{\partial P} \right)_{s,T} \frac{\partial P}{\partial s} + \left(\frac{\partial G}{\partial T} \right)_{s,P} \frac{\partial T}{\partial s} \right]. \quad (28)$$

The first term represents the driving force for an s -change via the change in the Hamiltonian. It can be evaluated as an ensemble average over Eq. (19), leading to

$$\frac{1}{\Delta N} \left(\frac{\partial G}{\partial s} \right)_{P,T} = \frac{1}{\Delta N} \left(\frac{\partial \mathcal{H}}{\partial s} \right) = 3s^{-1}\rho^{-1}\langle \mathcal{P} \rangle. \quad (29)$$

The second term represents the driving force for the s -change via the change in the pressure. It can be evaluated using Eq. (22), leading to

$$\frac{1}{\Delta N} \left(\frac{\partial G}{\partial P} \right)_{s,T} \frac{\partial P}{\partial s} = \frac{\Delta V}{\Delta N} (-3s^{-2}P^*) = -3s^{-1}\rho^{-1}P. \quad (30)$$

Finally, the third term vanishes in the absence of any s -dependence for the temperature. It follows that the total derivative of Eq. (28) is zero. Accordingly, there is no net driving force for the atoms to move along z ,

$$-\frac{d\mu(z)}{dz} = -\frac{d\mu(P, T, s)}{ds} \frac{ds}{dz} = F_t + \langle F_d \rangle = 0. \quad (31)$$

The first component is of thermodynamic nature, namely,

$$F_t = 3s^{-1}\rho^{-1}P \frac{ds}{dz} = -\rho^{-1} \frac{dP}{dz}. \quad (32)$$

It accounts for the effect of the pressure gradient and tends to drive atoms from higher to lower pressure (leading to pressure homogenization) or, equivalently, from lower scaling to higher scaling. The second component accounts for the mean effect of the drift force, which is given by

$$F_{d,i} = -\frac{\partial \mathcal{H}}{\partial s_i} \frac{ds_i}{dz} \quad \text{so that} \quad \langle F_d \rangle = -3s^{-1}\rho^{-1}\langle \mathcal{P} \rangle_z \frac{ds}{dz}. \quad (33)$$

On average, this force compensates the thermodynamic driving force, enabling an inhomogeneous pressure at equilibrium. Owing to this pressure heterogeneity maintained by the action of the drift force in the AdSoS setup, a volume element of CG solvent at scaling s is in equilibrium at the pressure $s^{-3}P^*$ that leads to the appropriate s -corrected density $s^{-3}\rho^*$. If a reference pressure (e.g., atmospheric) is specified for the system, it will only be relevant for the FG compartment. Because the pressure heterogeneity renders the barostating of the system non-trivial, the design of an AdSoS variant for NPT conditions is left for future work.

G. Density artifacts and correction potential

The FG and CG regions both involve a homogeneous s -value so that their properties are expected to scale according to Table I. In the SG region, the drift force along the z -axis compensates for the driving force related to the heterogeneous pressure profile. As a result, the AdSoS scheme should generate a nearly homogeneous profile for the scaled density $s^3\rho$, and provide an appropriate description of solvation for a possible solute embedded in the FG region.

In practice, however, the presence of s -variations in the system may still cause artifacts, which are expected to become increasingly pronounced for large s -gradients. Additional causes for such artifacts may include: (i) the use of an *ad hoc* geometric-mean rule to combine the s_i and s_j factors within the pairwise interactions [Eq. (25)]; (ii) specific close-range packing and orientation

alterations between the solvent molecules in (or close to) regions presenting s -variations; and (iii) the use of cutoff truncation in the calculation of the non-bonded interactions.

If desired, these artifacts can be eliminated by adding a biasing potential along the z -direction, as done in some implementations of AdResS⁸⁸ (note that the thermodynamic force,^{89,90} which is applied for this purpose in more recent versions of AdResS, is not derived from a potential energy function). In the present work, following the local-elevation umbrella-sampling (LEUS) approach,¹³⁴ this biasing potential is represented as a weighted sum of local basis functions centered at successive grid points along the z -axis. A first local-elevation¹³⁵ phase involves the non-equilibrium build-up of the biasing potential. A second umbrella-sampling phase¹³⁶ involves the equilibrium sampling of the system using a frozen biasing potential. Note that such a biasing potential is expected to be specific to a given AdSoS setup, i.e., on the following choices: solvent; value of s_{\max} ; sizes of the FG, CG, and SG compartments; and choice of the $s(z)$ function. It should be generated in the absence of solute, i.e., in the situation where a homogeneous scaled-density profile $s^3\rho$ is expected. The potential is then assumed to be portable from system to system (if the box dimensions and partitioning as well as the cutoff are preserved), i.e., applicable irrespective of the solute.

H. Integrator

The equations of motion for the AdSoS scheme are easily implemented in the form of a leap-frog integrator¹³⁷ involving the momenta. For propagating the coordinate and momentum vectors of a particle i over a time step Δt , given the force F_i of Eq. (26) [or Eq. (27)], this gives

$$\mathbf{p}_i(t + \Delta t/2) = \mathbf{p}_i(t - \Delta t/2) + \mathbf{F}_i(t)\Delta t$$

and

$$\mathbf{r}_i(t + \Delta t) = \mathbf{r}_i(t) + \frac{\mathbf{p}_i(t + \Delta t/2)}{m_i(t)}\Delta t, \quad (34)$$

where it is noted that the mass m_i is time-dependent. This dependence is due to the scaling of masses [Eq. (16)], which makes them depend on the position (and thus on time). Using the approximation

$$\mathbf{v}_i(t - \Delta t/2) = \mathbf{p}_i(t - \Delta t/2)/m_i(t - \Delta t) \quad (35)$$

and

$$\mathbf{v}_i(t + \Delta t/2) = \mathbf{p}_i(t + \Delta t/2)/m_i(t), \quad (36)$$

this leap-frog scheme can be rewritten for the integration in terms of velocities¹³⁸ as

$$\mathbf{v}_i(t + \Delta t/2) = \left(\frac{s_i(t)}{s_i(t - \Delta t)} \right)^2 \mathbf{v}_i(t - \Delta t/2) + \frac{\mathbf{F}_i(t)}{m_i(t)}\Delta t$$

and

$$\mathbf{r}_i(t + \Delta t) = \mathbf{r}_i(t) + \mathbf{v}_i(t + \Delta t/2)\Delta t. \quad (37)$$

The first term in the velocity equation ensures that a change in mass via a change in s is accompanied by a corresponding velocity adjustment leading to an unaltered momentum. Note that this integrator is only first-order accurate (error proportional to Δt) and not symplectic.¹³⁸ Symplectic integrators preserve the volume of phase space such that the system stays on the same manifold safe for numerical fluctuations.¹³⁹ As a consequence, symplecticity

guarantees a conserved system Hamiltonian, with fluctuations around its mean that increase with Δt .¹⁴⁰ The leap-frog integrator is only symplectic if the Hamiltonian is separable into a component that only depends on the positions, and a component that only depends on the momenta, in which case it is third-order accurate (error proportional to Δt^3). This is not true for the AdSoS scheme, where the kinetic energy couples the position and momentum coordinates. Although a symplectic integration scheme for such non-separable Hamiltonians has been proposed,¹⁴¹ its underlying mechanism involves simulating two replicas, which would be detrimental to the computational efficiency of AdSoS. The integration scheme of Eq. (37) is expected to cause an energy drift in NVE simulations that scales linearly with the time step.

Because the scaling isomorphism preserves time, two homogeneously scaled systems at different s -values will lead to trajectories where the successive frames are scaled versions of each other if the same time step Δt is used in both cases. This feature is also expected to hold qualitatively in an AdSoS setup. Thus, provided that the s -gradients are reasonably low, the time step appropriate for an accurate integration of the FG model will produce a similarly accurate integration in the SG and CG region.

A thermostat can easily be added to the integrator of Eq. (37) as the reference temperature T_{ref} and its coupling time τ_T are not affected by the scaling. Using the Berendsen thermostat,¹⁴² the velocities $v(t + 1/2\Delta t)$ merely need to be rescaled with a factor α , given by

$$\alpha \left(t + \frac{\Delta t}{2} \right) = \left[1 + \frac{\Delta t}{\tau_T} \left(\frac{T_{\text{ref}}}{T(t + \frac{\Delta t}{2})} - 1 \right) \right]^{1/2}. \quad (38)$$

III. METHODS

The AdSoS scheme in slab geometry (without solute) for an atomic liquid with Lennard-Jones and Coulomb interactions was implemented in a GROMOS-compatible simulation engine written in C++ (SAMOS¹⁴³). This implementation relied on the geometry of Fig. 2, the Hamiltonian of Eq. (25), the forces of Eq. (27), and the modified leap-frog integrator of Eq. (37). In a preliminary step, simulations were also performed for systems with a homogeneous scaling, i.e., a fixed s -value throughout the computational box, and the Hamiltonian of Eqs. (7)–(9). All floating-point operations were carried out in double precision to limit the noise induced by numerical errors.

The atomic liquid considered was argon at $T = 87$ K, with the atomic mass $m^* = 39 \text{ g mol}^{-1}$ and the square-root Lennard-Jones coefficients $c_6^* = 0.07915 \text{ kJ mol}^{-1} \text{ nm}^{-3}$ and $c_{12}^* = 3.138 \cdot 10^{-3} \text{ kJ mol}^{-1} \text{ nm}^{-6}$ (taken from the GROMOS 54A7 force field¹⁴⁴) at the FG level. Most simulations involved an atomic charge $q^* = 0$, as appropriate for liquid argon. To test the scheme for Coulomb interactions, additional simulations were performed for a hypothetical

argon-based ionic liquid with atomic charges $q^* = \pm 0.05 e$ at the FG level. The reference number density for the uncharged FG model, as evaluated by an independent NPT simulation at 87 K and 1 bar, is $\rho^* = 20.7 \text{ nm}^{-3}$. The same value was used as a reference for the ionic liquid. All simulations were carried out under periodic boundary conditions and, unless otherwise specified, at a constant volume. For comparison, preliminary simulations with homogeneous scaling were also performed at a constant pressure of 1 bar.

A. Simulations of liquid argon with homogeneous scaling

A series of simulations of liquid argon with homogeneous scaling was carried out to test the validity of the isomorphism relating the FG system to CG systems constructed by scaling. To this purpose, nine s -values ranging from 1 to 5 in steps of 0.5 were considered, with $s = 1$ corresponding to the FG system. For each s -value, the force-field parameters were scaled according to Eq. (16), leading to CG models with graining levels N_G ranging from 1 to 125. The corresponding initial configurations were generated by performing a scaling according to Eq. (6), starting from a common computational box containing 1000 FG argon atoms pre-equilibrated at number density ρ^* . Note that the initial velocities are scaled by s (following from the scaling of the mass by s^{-2} and of the momenta by s^{-1}) and that the number density becomes $s^{-3}\rho^*$ [Eq. (21)].

Two sets of simulations were then performed considering the nine different s -values under either NVT or NPT conditions. In both cases, the temperature was maintained close to 87 K using a weak-coupling thermostat¹⁴² [Eq. (38)] with a coupling time of 0.1 ps. In the latter case, the pressure was maintained close to 1 bar using a weak-coupling barostat¹⁴² with a coupling time of 0.5 ps and a compressibility κ^* of 0.0578 bar^{-1} . The latter value corresponds to the uncharged FG model and was evaluated based on independent liquid simulations at different pressures. The pairwise interactions were evaluated at every step and truncated at a cutoff distance \tilde{R}_c , which scaled with s according to Eq. (20), with a R_c^* value of 1.4 nm at the FG level. The integration time step was set to 2 fs, and each system was simulated for 1 ns.

To assess the effect of Coulomb interactions in the system, a corresponding set of simulations (NVT and NPT) was performed for a hypothetical argon-based ionic liquid, with charges of $\pm 0.05 e$ on the atoms.

B. AdSoS simulations of liquid argon

For the AdSoS simulations of liquid argon in the slab setup of Fig. 2, the dependence of the scaling factor s on the position along z is represented using a piecewise-linear function, as illustrated in Fig. 3(a) (see also Appendix B for alternative choices). The corresponding mathematical expression is

$$s(z) = \begin{cases} 1, & z \leq \frac{1}{2}d_{\text{FG}} \text{ or } z \geq L_z - \frac{1}{2}d_{\text{FG}}, \\ 1 + \frac{s_{\text{max}} - 1}{d_{\text{SG}}} \left(z - \frac{1}{2}d_{\text{FG}} \right), & \frac{1}{2}d_{\text{FG}} < z < \frac{1}{2}d_{\text{FG}} + d_{\text{SG}}, \\ s_{\text{max}}, & \frac{1}{2}d_{\text{FG}} + d_{\text{SG}} \leq z \leq L_z - \frac{1}{2}d_{\text{FG}} - d_{\text{SG}}, \\ 1 + \frac{s_{\text{max}} - 1}{d_{\text{SG}}} \left(L_z - z - \frac{1}{2}d_{\text{FG}} \right), & L_z - \frac{1}{2}d_{\text{FG}} - d_{\text{SG}} < z < L_z - \frac{1}{2}d_{\text{FG}}, \end{cases} \quad (39)$$

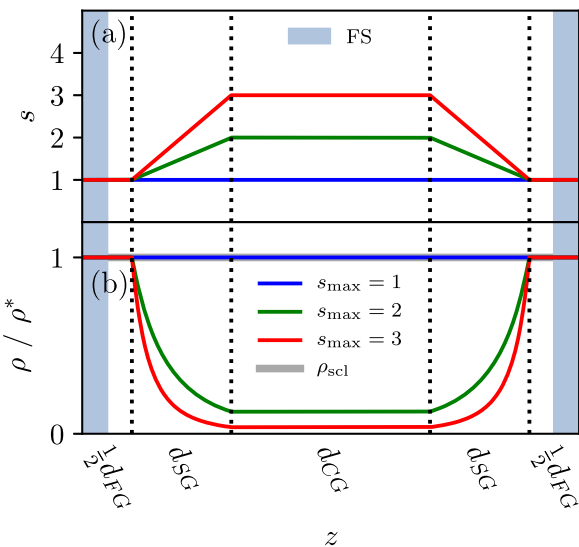


FIG. 3. Schematic illustration of the box partitioning, position-dependent scaling factor, and expected density profiles in AdSoS simulations with three different values of s_{\max} . (a) The position-dependent scaling factor $s(z)$ as given by Eq. (39) and (b) the relative number density $\rho(z)/\rho^*$, where ρ^* is the number density of the FG model. The latter quantity is expected to scale with s^{-3} so that the scaled density ρ_{scl} [Eq. (41), thick gray line] should have a uniform value of one along the entire z -range, irrespective of the choice of s_{\max} . The figure also illustrates a hypothetical FG solute (FS) region as the central half of the FG region (blue strips, $z \leq \frac{1}{4}d_{\text{FG}}$ and $z \geq L_z - \frac{1}{4}d_{\text{FG}}$), used in the analysis of the simulations to estimate the long-range solvation energy in the AdSoS setup.

where d_{FG} , d_{SG} , and d_{CG} are the widths of the FG region, the two SG regions, and the CG region, respectively, L_z is the box-edge length in the z -direction, and s_{\max} is the maximum scaling factor (defining the resolution of the CG region).

Five s_{\max} values ranging from 1 (system entirely FG) to 3 (CG model with $N_G = 27$) in steps of 0.5 were considered. The box dimensions and partitioning were kept identical for all choices of s_{\max} , with $L_x = L_y = 7$ nm, $L_z = 10$ nm, $d_{\text{FG}} = 2$ nm, $d_{\text{SG}} = 2$ nm, and $d_{\text{CG}} = 4$ nm. The number of atoms N was determined for each value of s_{\max} according to

$$N = L_x L_y \rho^* \int_0^{L_z} s^{-3}(z) dz, \quad (40)$$

with rounding of the result to the closest even integer. The values of N range between 10 144 atoms for $s_{\max} = 1$ and 3080 atoms for $s_{\max} = 3$ (see Tables IV and V in Sec. IV). Increasing s_{\max} leads to a smaller number of atoms in the CG and SG regions and to larger s -gradients in the SG regions. The values of L_x and L_y were selected in such a way that the CG region still contains about 150 atoms for $s_{\max} = 3$. For each value of s_{\max} , initial configurations were prepared by randomly placing the appropriate number N of atoms in the computational box, followed by energy minimization and 50 ps equilibration at 87 K using temperature constraining.^{145–147}

Two sets of simulations were performed considering the five different choices of s_{\max} and involving either NVE or NVT conditions. The NVE simulations were carried out for 100 ps using three different time steps of 0.5, 1, or 2 fs. The NVT simulations were performed for a duration of 1 ns using a time step of 2 fs. The

temperature was maintained close to 87 K using a weak-coupling thermostat¹⁴² [Eq. (38)] with a coupling time of 0.1 ps. For all simulations, the non-bonded interactions were truncated using a minimum-image convention (no cutoff).

The NVE simulations were only used to assess energy conservation. The NVT simulations were analyzed in terms of property profiles and energy components. Density profiles $\rho(z)$ along the z -axis were extracted from the coordinate trajectories using a bin width of 0.05 nm. Assuming that there is no thermodynamic mismatch between regions at different scalings (and in the absence of a solute), this function should depend on z as $\rho(z) = s^{-3}(z)\rho^*$ [Eq. (21)], as illustrated by $\rho(z)/\rho^*$ in Fig. 3(b). In practice, it is convenient to consider the scaled density profile

$$\rho_{\text{scl}}(z) = s^3(z)\rho(z)/\rho^*, \quad (41)$$

which is expected to present a uniform value of one over the entire box in an ideal pure-solvent situation. Temperature profiles $T(z)$, which were constructed on-the-fly using a bin width of 0.1 nm, were also extracted. Defining a hypothetical FG solute region (FS) as the central half of the FG region (blue strips in Fig. 3), interaction energies between the FS and the SG+CG regions were monitored as an estimate for the long-range solvation energy of this hypothetical solute in the AdSoS setup. This interaction energy was partitioned in terms of the different non-bonded contributions, and standard errors on these quantities were estimated by block-averaging.¹⁴⁸

C. AdSoS simulations of an argon-based ionic liquid

To investigate the effect of Coulomb interactions in the system, the AdSoS simulations of Sec. III B were repeated considering a hypothetical argon-based ionic liquid. For this, the argon atoms were assigned a charge q^* of $\pm 0.05 e$ at the FG level, positive for half of the atoms and negative for the other half [allowed by the rounding of N to an even number in Eq. (40)]. The magnitude of the charges is sufficiently low to prevent crystallization and avoid artifacts resulting from the lack of a long-range correction for the electrostatic interactions (i.e., beyond the applied minimum-image truncation). The setup and analysis of these simulations are otherwise identical to those of the corresponding simulations for the uncharged liquid argon.

D. Correction of density artifacts with a biasing potential

A series of AdSoS simulations were performed to investigate the feasibility of correcting residual artifacts in the density profiles using a biasing potential constructed according to the LEUS scheme.¹³⁴ These simulations were performed for both liquid argon and the argon-based ionic liquid, and relied on $s_{\max} = 2$ (CG model with $N_G = 8$). Two important modifications in the setup led to a more practically relevant situation. First, the non-bonded interactions were truncated using a spherical cutoff $R_c = 2.8$ nm (instead of a minimum-image convention). Second, the simulations of the ionic liquid relied on reaction-field electrostatics^{149,150} with conducting boundary $\epsilon_{\text{RF}} = \infty$ (instead of plain Coulomb interactions).

The biasing potential covered a z -range from 0 to $L_z/2$ and was applied symmetrically with respect to the midpoint of the box (center of the CG region; see Fig. 2). It was constructed as a weighted sum of local truncated-polynomial functions¹⁵¹ (see Appendix A

therein) centered at successive grid points with a spacing of 0.1 nm. The local-elevation phase lasted 2 ns and involved a force-constant increment per visit of 10^{-2} kJ mol $^{-1}$, where the contribution of a given atom was weighted by s^3 in order to arrive at a homogeneous scaled density ρ_{sc} , as given in Eq. (41). The umbrella-sampling phase lasted 1 ns, and relied on a frozen biasing potential defined as an average over the last 1.9 ns of the build-up phase.

IV. RESULTS AND DISCUSSION

A. Simulations of liquid argon with homogeneous scaling

The results for the simulations of liquid argon with homogeneous scaling under both NVT and NPT conditions are reported in Table II for five different integer s -values. The results for the average pressure P (NVT) and for the average s -corrected density $s^3\rho_{\text{NPT}}$ (NPT) are shown graphically in Fig. 4 (also including half-integer s -values).

Under NVT conditions, the simulations performed at different s -values, which were initiated by scaling the same FG configuration, are expected to evolve along rigorously isomorphic trajectories. This means that scaling the initial condition as $\mathbf{r}(0) = s\mathbf{r}^*(0)$ and $\mathbf{v}(0) = s\mathbf{v}^*(0)$ should imply that at all times t , $\mathbf{r}(t) = s\mathbf{r}^*(t)$ and $\mathbf{v}(t) = s\mathbf{v}^*(t)$. In addition, all energetic quantities should be unaffected. This is indeed the case for the total potential energies U_{pot} with $s \leq 2$ (Table II). For the higher s -values, small deviations are observed, which can be traced back to a divergence in the trajectories after a few thousand steps caused by finite numerical precision. Note that if the isomorphism is demonstrated here under NVT conditions (with the proviso of possible numerical deviations), it also holds for simulations under NVE conditions, i.e., in the absence of thermostating (with the same proviso).

The evolution $P(s)$ of the pressure as a function of the scaling factor s under NVT conditions is displayed in Fig. 4(a), together with the analytical curve from Eq. (22) with $P^* = 5.18$ bar. Note that the latter pressure, which corresponds to the FG model ($s = 1$), is somewhat above 1 bar. This results from the very high sensitivity of the pressure to the exact density ρ^* selected when setting up the computational box (i.e., ρ^* is in fact slightly above the density of

TABLE II. Results for the simulations of liquid argon with homogeneous scaling under NVT and NPT conditions. The reported values are the total potential energy U_{pot} (NVT), the average pressure P (NVT), and the average s -corrected number density $s^3\rho_{\text{NPT}}$. The potential energies and s -corrected densities have statistical errors on the order of 10^{-1} kJ mol $^{-1}$ and 10^{-3} nm $^{-3}$, respectively, as estimated by block-averaging¹⁴⁸ (the statistical error on the pressure amounts to about 7% of its magnitude).

s	U_{pot} (NVT) (kJ mol $^{-1}$)	P (NVT) (bar)	$s^3\rho_{\text{NPT}}$ (NPT) (nm $^{-3}$)
1	-5807.4	5.18	20.677
2	-5807.4	0.65	20.714
3	-5807.2	0.21	20.801
4	-5807.2	0.09	20.959
5	-5807.3	0.04	21.204

the liquid argon model at 1 bar). As expected, the pressure scales with the inverse-cube of s . Again, slight deviations from the analytical expression are due to trajectory divergences caused by finite numerical precision.

The evolution of the s -corrected density $s^3\rho_{\text{NPT}}(s)$ as a function of the scaling factor s under NPT conditions at a reference pressure P_{ref} set to 1 bar is displayed in Fig. 4(b), together with a curve corresponding to Eq. (24) with $P^* = 1$ bar, $\rho^* = 20.7$ nm $^{-3}$ and $\kappa^* = 0.0578$ bar $^{-1}$. The latter expression provides a first-order approximation to the density change resulting from the pressure change from $s^{-3}P^*$ to P_{ref} . This corresponds to an increasingly strong compression upon increasing s . As a result, the s -corrected density increases with s . This change is well described by Eq. (24) for low s -values. At high s -values, deviations relative to this estimate become more important due to the influence of higher-order contributions.

B. Simulations of an argon-based ionic liquid with homogeneous scaling

The results for the simulations of the argon-based ionic liquid with homogeneous scaling under both NVT and NPT conditions are reported in Table III for five different integer s -values. The results for the average pressure P (NVT) and for the average s -corrected

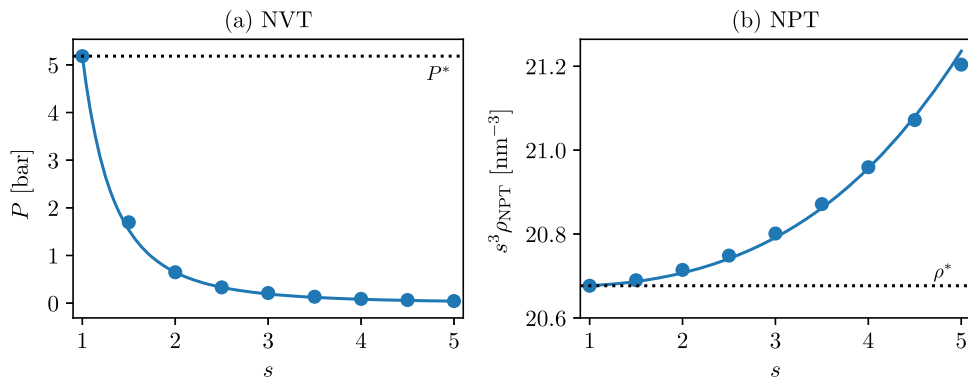


FIG. 4. Pressure (NVT conditions) or s -corrected density (NPT conditions) upon system scaling of liquid argon. (a) Pressure $P(s)$ as a function of the scaling factor s under NVT conditions, where the individual points are from the simulations and the curve corresponds to Eq. (22) with $P^* = 5.18$ bar, and (b) s -corrected number density $s^3\rho_{\text{NPT}}(s)$ as a function of the scaling factor s under NPT conditions, where the individual points are from the simulations and the curve corresponds to Eq. (24) with $P^* = 1$ bar and $\rho^* = 20.7$ nm $^{-3}$ and $\kappa^* = 0.0578$ bar $^{-1}$. The results from the simulations are reported numerically in Table II.

TABLE III. Results for the simulations of the argon-based ionic liquid with homogeneous scaling under NVT and NPT conditions. The reported values are the total potential energy U_{pot} (NVT), the average pressure P (NVT), and the average s -corrected number density $s^3 \rho_{\text{NPT}}$ (NPT). The potential energies have statistical errors on the order of 1 kJ mol^{-1} as estimated by block-averaging¹⁴⁸ (the statistical errors on the pressure and the s -corrected densities amount to about 3% and 0.02% of their magnitudes, respectively).

s	U_{pot} (NVT) (kJ mol^{-1})	P (NVT) (bar)	$s^3 \rho_{\text{NPT}}$ (NPT) (nm^{-3})
1	-6349	-39.13	20.893
2	-6351	-5.40	20.915
3	-6349	-1.52	21.010
4	-6346	-0.64	21.160
5	-6348	-0.31	21.370

density $s^3 \rho_{\text{NPT}}$ (NPT) are shown graphically in Fig. 5 (also including half-integer s -values). Note that the NVT simulations were carried out at the same density ρ^* as used previously for liquid argon.

The results are qualitatively similar to those for the neutral liquid, quantitative differences arising from the inclusion of (overall attractive) electrostatic interactions. The potential energy is significantly lower than for the neutral liquid. The results corresponding to different s -values under NVT conditions are comparable, with small deviations resulting from numerical errors that cause the trajectories to diverge. The larger deviations compared to the neutral liquid may be related to the more pronounced influence of cutoff effects in the presence of long-range Coulomb interactions.

Due to the attractive interactions and the use of the same reference density as for the neutral liquid, the pressure under NVT conditions is negative. It also scales as s^{-3} . Under NPT conditions, the scaled density is expectedly somewhat higher than in the pure liquid case, and increases with s . Note that the fit in Fig. 5(b) is performed using the compressibility of the neutral liquid, which results in discrepancies at high s -values.

C. Number of particles in the AdSoS simulations

Given the use of identical sizes for the FG region, the two SG regions, and the CG region of the computational box (Fig. 2) in the

TABLE IV. Energy and energy component analysis for the AdSoS simulations of liquid argon with s_{max} ranging from 1 to 3 in steps of 0.5. For each s_{max} value, the different columns report the total number N of atoms in the box given by Eq. (40) (applied with rounding to the closest even integer), the total potential energy $u_{\text{tot}} = N^{-1} U_{\text{tot}}$ per atom, the long-range dispersive component U_6^{sol} to the solvation of a hypothetical solute, and the corresponding long-range repulsive component U_{12}^{sol} . The hypothetical solute region corresponds to the solvent atoms in the FS region (Fig. 3), and the long-range solvation refers to the interaction energy of these atoms with those in the SG and CG regions (Fig. 2). Error estimates calculated using block-averaging¹⁴⁸ are on the order of magnitude of $\pm 10^{-4}$, $\pm 10^{-1}$, and $\pm 10^{-3}$, respectively, for u_{tot} , U_6^{sol} , and U_{12}^{sol} .

s_{max}	N	u_{tot} (kJ mol^{-1})	U_6^{sol} (kJ mol^{-1})	U_{12}^{sol} (kJ mol^{-1})
1.0	10 144	-5.9044	-241.2	0.896
1.5	5 484	-5.8985	-239.7	0.928
2.0	4 056	-5.8924	-238.6	0.962
2.5	3 424	-5.8896	-240.0	1.014
3.0	3 080	-5.8864	-241.5	1.073

different simulations, the number N of atoms required to fill this box [Eq. (40)] decreases with the scaling factor s_{max} defining the resolution in the CG region. The corresponding values are reported in Tables IV and V (identical for the liquid argon and argon-based ionic liquid). The number N decreases rapidly upon increasing s_{max} . For the selected system geometry, the FG region occupies 20% of the total volume, which imposes a lower bound of about 2030 FG atoms, corresponding to the limit of N when s_{max} becomes very large. The upper bound of 10 144 atoms corresponds to the system represented fully at FG resolution, i.e., with $s_{\text{max}} = 1$. This number is already reduced by about a factor of 2 with $s_{\text{max}} = 1.5$ (maximal graining level N_G of about 3.4) and by about a factor of 3 with $s_{\text{max}} = 3$ (N_G of 27). If an efficient algorithm is used for the calculation of the pairwise interactions, i.e., achieving (nearly) linear scaling with the system size, the reduction factor in terms of the number of atoms is expected to provide an equivalent reduction in terms of computational cost.

D. AdSoS simulations of liquid argon

The scaled density and the temperature profiles under NVT conditions, as well as the energy drifts under NVE conditions, are

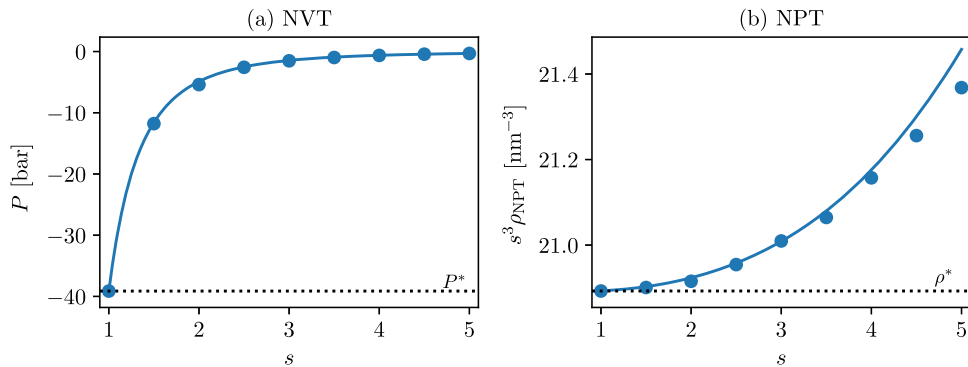


FIG. 5. (a) Pressure (NVT conditions) and (b) s -corrected density (NPT conditions) upon system scaling of the argon-based ionic liquid. Panels (a) and (b) are analogous to Fig. 4. In (a), $P^* = -39$ bar, which is significantly lower compared to the neutral argon (where $P^* = 5.18$ bar) due to the attractive nature of the electrostatic interactions.

TABLE V. Energy and energy component analysis for the AdSoS simulations of the argon-based ionic liquid with s_{\max} ranging from 1 to 3 in steps of 0.5. For each s_{\max} value, the different columns report the total number N of atoms in the box given by Eq. (40) (applied with rounding to the closest even integer), the total potential energy $U_{\text{tot}} = N^{-1} U_{\text{tot}}$ per atom, the electrostatic component $U_{\text{ele}}^{\text{sol}}$ to the solvation of a hypothetical solute, the corresponding long-range dispersive component U_6^{sol} , and the corresponding long-range repulsive component U_{12}^{sol} . The hypothetical solute region corresponds to the solvent atoms in the FS region (Fig. 3), and the long-range solvation refers to the interaction energy of these atoms with those in the SG and CG regions (Fig. 2). Error estimates calculated using block-averaging¹⁴⁸ are on the order of magnitude of $\pm 10^{-4}$, ± 1 , $\pm 10^{-1}$, and $\pm 10^{-3}$, respectively, for U_{tot} , $U_{\text{ele}}^{\text{sol}}$, U_6^{sol} , and U_{12}^{sol} .

s_{\max}	N	U_{tot} (kJ mol ⁻¹)	$U_{\text{ele}}^{\text{sol}}$ (kJ mol ⁻¹)	U_6^{sol} (kJ mol ⁻¹)	U_{12}^{sol} (kJ mol ⁻¹)
1.0	10 144	-6.4468	0.2	-241.2	0.898
1.5	5 484	-6.4415	0.7	-239.1	0.924
2.0	4 056	-6.4351	2.4	-239.7	0.973
2.5	3 424	-6.4324	2.1	-239.7	1.010
3.0	3 080	-6.4289	3.8	-241.1	1.068

shown in Fig. 6 for the AdSoS simulations of liquid argon with $s_{\max} = 1$, 2, or 3. Since the thermodynamic force (due to the inhomogeneous pressure profile along the z -axis) and the drift force (due to the position dependence of the Hamiltonian via s in the presence of an s -gradient) compensate each other on average, the scaled densities $\rho_{\text{sc}}[z]$ [Eq. (41)] are expected to be homogeneous at a value of one throughout the entire z -range [Fig. 3(b)]. This compensation is only expected to hold in a strict fashion in the limit of small s -gradients.

As can be seen in Fig. 6(a), ρ_{sc} is indeed very close to one throughout the box (oscillations on the order of 1%) in the fully FG situation ($s_{\max} = 1$, no solvent-scaling involved). However, artifacts appear for the choices $s_{\max} = 2$ or 3, which involve negative deviation peaks at the FG-SG boundaries and positive deviation peaks at the CG-SG boundaries, as well as slight positive deviations over the SG regions. The magnitudes of the peaks are about 8% for $s_{\max} = 2$ (maximal grainings N_G of 8) and 15%–25% for $s_{\max} = 3$ (maximal N_G of 27). These peaks probably result from the stepwise change in the derivative of the s -gradient at the FG-SG and CG-SG boundaries, and from potential preferential-packing effects, which tighten or loosen the arrangement of spherical particles at specific ratios of van der Waals radii. The effect of different choices of $s(z)$ on these density artifacts is discussed in Appendix B. Despite these artifacts in the SG region and at its boundaries, a homogeneous scaled density very close to one is still achieved in the FG and CG compartments for all s_{\max} , suggesting that AdSoS might still account appropriately for short- and long-range solvation. In addition, as will be shown further below, these artifacts can be eliminated using an appropriate biasing potential.

The solvent-scaling involved in the AdSoS scheme does not alter the temperature. As a result, the temperature profiles $T(z)$ are expected to be homogeneous over the entire z -range. As can be seen in Fig. 6(b), $T(z)$ is very close to 87 K throughout the box (with variations/oscillations on the order of 0.5 K) in the fully FG situation ($s_{\max} = 1$, no solvent-scaling involved). For the choices $s_{\max} = 2$ or 3, the variations in $T(z)$ are on the same order of magnitude, although the oscillations in the CG compartment (and in the SG compartments close to the CG region) are noticeably larger, especially for $s_{\max} = 3$. This increase is related to the smaller number of particles in these regions upon increasing s_{\max} , leading to poorer statistics at finite simulation time. Besides this effect, the comparison shows

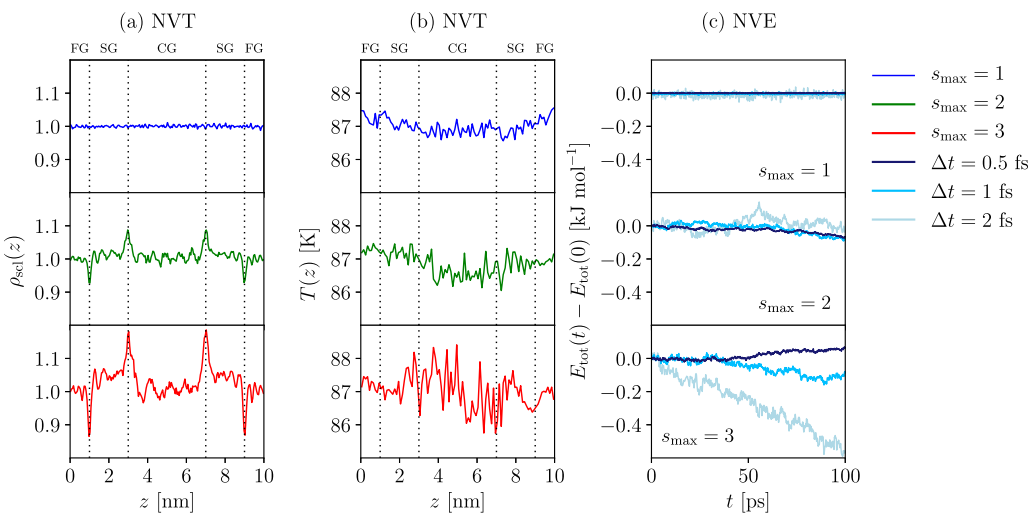


FIG. 6. Scaled density and temperature profiles (NVT) as well as energy drifts (NVE) for the AdSoS simulations of liquid argon with $s_{\max} = 1$, 2, or 3. For each value of s_{\max} (lines), panels (a)–(c) (columns) display (a) the scaled density profile ρ_{sc} [Eq. (41)] along the z -axis of the box in the NVT simulation, (b) the temperature profile $T(z)$ along the z -axis of the box in the NVT simulation, and (c) the time series of the change in total energy (total energy minus that of the first configuration) corresponding to three different choices of integration time steps in the NVE simulations. For the NVT simulations, the reference density is $\rho^* = 20.7 \text{ nm}^{-3}$, the reference temperature is 87 K, and the integration time step is 2 fs. The NVE simulations were initiated from a configuration equilibrated under the NVT conditions.

that the AdSoS modification of the dynamics does not induce any artificial temperature heterogeneities.

The integrator of Eq. (37) is expected to be accurate to the third order in Δt for $s_{\max} = 1$ and to the first order only for $s_{\max} > 1$. This is in line with the increase in the energy drift with Δt for $s_{\max} = 2$ and 3 in Fig. 6(c), whereas only the energy fluctuations increase upon increasing the time step for the fully FG system. Note that the magnitudes of these drifts remain in all cases extremely small relative to the total energy of the system (about -48 , -19 , and $-15 \cdot 10^3$ kJ mol $^{-1}$ for $s_{\max} = 1$, 2, or 3, respectively). These energy drifts decrease when the integration time step is reduced, which implies the absence of a systematic (zeroth-order) integration error.

The average potential energy u_{tot} per atom, as well as the dispersive and repulsive components U_6^{sol} and U_{12}^{sol} of the long-range solvation energy of a hypothetical FG solute, (interaction of atoms in the FS region of Fig. 3 with atoms in the SG and CG region), are reported in Table IV for AdSoS simulations with s_{\max} values ranging between 1 and 3 in steps of 0.5.

As the solvent-scaling is constructed to preserve the energetic quantities, the contribution of any atom to the total potential energy of the system should in principle be independent of its scaling factor. Here again, this property is only expected to hold in a strict fashion in the limit of small s -gradients. In practice, the value of u_{tot} decreases in magnitude upon increasing the value of s_{\max} . However, the change is extremely small, at most about 0.3% when s_{\max} is changed from 1 to 3 (change in N_g from 1 to 27).

Finally, the definition of a hypothetical solute region permits to test whether the long-range contribution to the dispersive solvation is properly accounted for in the AdSoS setup. The values

U_6^{sol} are very close to each other, irrespective of s_{\max} , with a slight non-monotonic trend (decrease in magnitude between 1 and 2 and increase in magnitude between 2 and 3). The magnitude of the variation only represents about 1% of U_6^{sol} , supporting the conservation of the long-range dispersive solvation upon scaling in AdSoS. In contrast, the repulsive contribution increases with s_{\max} because the volumetric repulsive component is expected to increase as s^3 upon solvent-scaling (factor s^6 for the interaction and factor s^{-3} for the density). Indeed, the value of U_{12}^{sol} increases systematically with s_{\max} . The change is important in relative terms, amounting to an increase by about 24% between s_{\max} values of 1 and 3. However, due the short-ranged nature of the repulsive term in r^{-12} , its contribution (and the associated change) is negligible compared to the dispersive component. For small s_{\max} , it will result in a slightly underestimated solvation of the FG solute. In the limit of extremely high s_{\max} , one could imagine that these repulsive forces induce a spurious density increase in the CG region. Note, however, that the U_{12}^{sol} values are not representative for the repulsive interactions within the CG region, which are subject to the (near) isomorphism, i.e., the balance between attractive and repulsive forces in this region is similar irrespective of s_{\max} .

E. AdSoS simulations of an argon-based ionic liquid

The scaled density and the temperature profiles under NVT conditions, as well as the energy drifts under NVE conditions, are shown in Fig. 7 for the AdSoS simulations of the argon-based ionic liquid (charges $q^* = \pm 0.05e$ on the atoms at the FG level) with $s_{\max} = 1$, 2, or 3. The $\rho_{\text{sc}}(z)$ and $T(z)$ profiles for the ionic liquid under NVT conditions, as well the energy drifts under NVE conditions, are very similar to those obtained for liquid argon in Fig. 6,

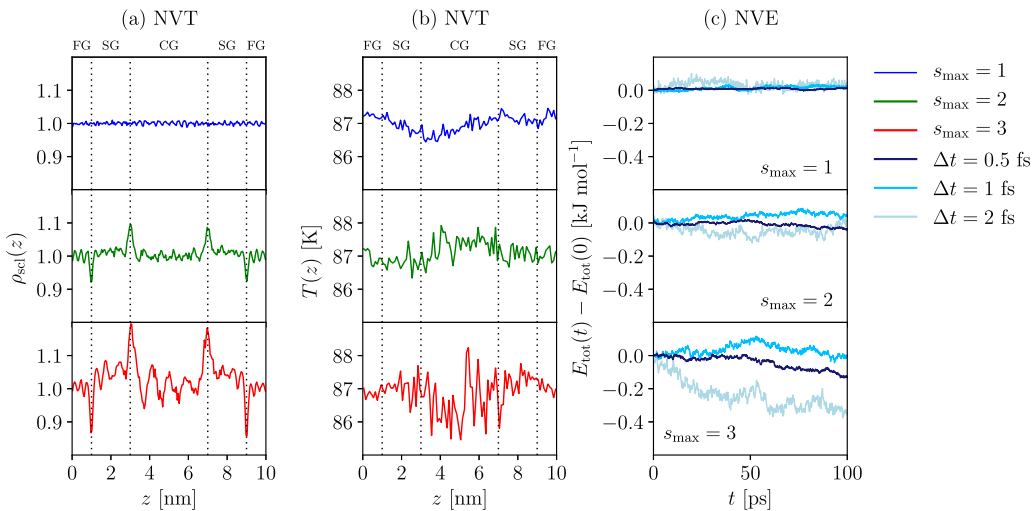


FIG. 7. Scaled density and temperature profiles (NVT) as well as energy drifts (NVE) for the AdSoS simulations of the argon-based ionic liquid with $s_{\max} = 1$, 2, or 3. For each value of s_{\max} (lines), panels (a)–(c) (columns) display (a) the scaled density profile ρ_{sc} [Eq. (41)] along the z -axis of the box in the NVT simulation, (b) the temperature profile $T(z)$ along the z -axis of the box in the NVT simulation, and (c) the time series of the drift in total energy (total energy minus that of the first configuration) corresponding to three different choices of integration time step in the NVE simulations. For the NVT simulations, the reference density is $\rho^* = 20.7$ nm $^{-3}$, the reference temperature is 87 K, and the integration time step is 2 fs. The NVE simulations were initiated from a configuration equilibrated under the NVT conditions.

suggesting that the same qualitative conclusions can be drawn in the presence of electrostatic interactions in the system.

The average potential energy u_{tot} per atom, as well as the electrostatic, dispersive, and repulsive components $U_{\text{ele}}^{\text{sol}}$, U_6^{sol} , and U_{12}^{sol} of the long-range solvation energy of a hypothetical FG solute, are reported in Table V. The value of u_{tot} is lower compared to that of liquid argon (Table IV) due to the inclusion of Coulomb interactions that are favorable on average. Again, the magnitude of u_{tot} decreases slightly upon increasing the value of s_{max} by about 0.3% when s_{max} is changed from 1 to 3. Thus, the Coulomb interactions satisfy the expected invariance of energy quantities, just as was the case for the Lennard-Jones interactions.

Similarly to liquid argon, the values U_6^{sol} are very close to each other with a slight non-monotonic trend (variation limited to about 1%), and the repulsive contribution U_{12}^{sol} increases systematically with s_{max} (increase by 19%) but remains small in magnitude. The values of $U_{\text{ele}}^{\text{sol}}$ are affected by large errors but appear to be small and positive, suggesting a slightly unfavorable electrostatic solvation of the FG solute region. In addition, this component increases systematically with s_{max} . This finding suggests that the electrostatic component of the long-range solvation may not be appropriately described for an ionic liquid because the free charges scale as $s^{1/2}$. A correct scaling is expected for the dielectric solvation by a molecular liquid, but not necessarily for the free-charge solvation by an ionic liquid. The sign and trend in $U_{\text{ele}}^{\text{sol}}$ may also in part be related to the density artifacts at the FG-SG and CG-SG boundaries, and to the fact that the scaling of individual atomic charges by $s^{1/2}$ may lead to a slight (time-dependent) violation of

the system electroneutrality. In the context of a molecular dipolar solvent (e.g., water), such electroneutrality violations can be avoided by performing the scaling on a per-molecule (rather than per-atom) basis.

F. Correction of density artifacts with a biasing potential

Although the AdSoS setup is expected to keep the thermodynamic mismatches in the system to a minimum (near-ideal mixing properties of scaled atoms at comparable s -values, continuous change of s with position, and appropriate pressure variations enabled by the drift force), density artifacts may still occur. As seen in Secs. IV D and IV E, these artifacts affect nearly exclusively the SG region as well as the FG-SG and CG-SG interfaces, and are enhanced by strong s -gradients in the SG regions. In contrast, the densities in the homogeneous CG and FG regions as well as the interaction energies do not appear to be significantly altered. In the following, it is shown that the residual density artifacts can be essentially eliminated by means of a biasing potential. In addition, the minimum-image cutoff used in the previous tests is replaced by a spherical-cutoff truncation, as would be used in practical applications of the method, and the truncation of electrostatic interactions is damped using a reaction-field correction.^{149,150}

Figures 8(a) and 8(b) show the scaled density profile and the applied biasing potential for liquid argon with $s_{\text{max}} = 2$. In the unbiased case (red curve), the CG and FG densities are offset by about 2% in comparison to the minimum-image setup of Fig. 6(a).

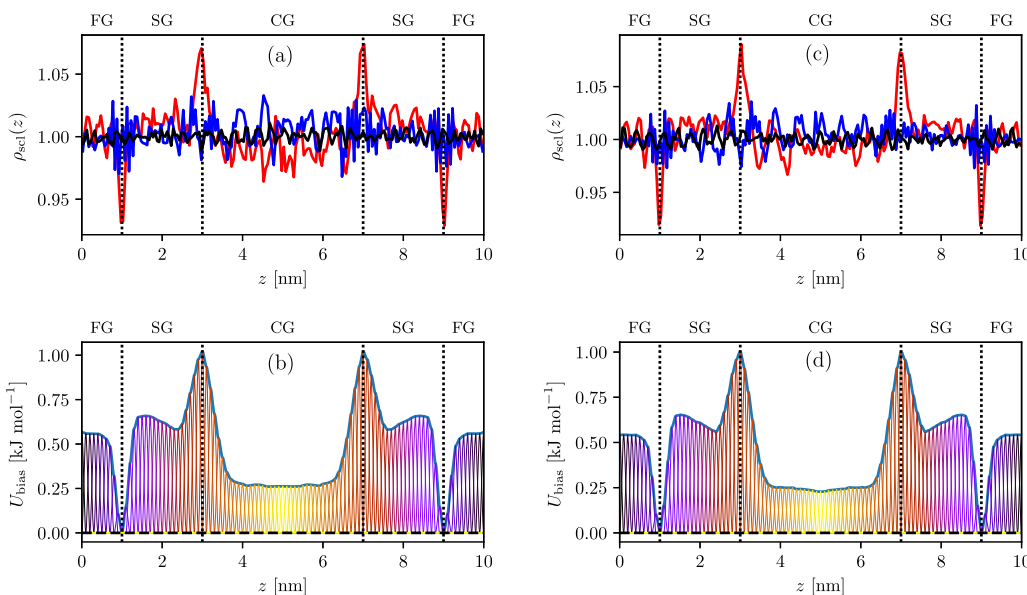


FIG. 8. Scaled density profiles and applied biasing potentials in the AdSoS simulations of liquid argon and the argon-based ionic liquid with $s_{\text{max}} = 2$. For liquid argon [(a) and (b)] and the argon-based ionic liquid [(c) and (d)], (a) and (c) show the scaled density profile ρ_{sc} [Eq. (41)] along the z-axis of the box in a simulation without (red curve) or with (blue curve) biasing potential, as well as the density profile in the reference fully FG system with $s_{\text{max}} = 1$ (black curve), while (b) and (d) show the biasing potential applied to the system involving biasing. In the representation of the biasing potential, the kernel functions are shown in a color spectrum ranging from yellow to violet. The enveloping blue curve corresponds to the sum of these kernel functions. Note that the biasing potential covers a z-range from 0 to $L_z/2$ and is applied symmetrically with respect to the midpoint of the box (center of the CG region; see Fig. 2).

When using a single cutoff distance for the entire system, the tail of the dispersive interactions, which is omitted, will have a larger magnitude for the CG particles compared to the FG particles. As a result, one observes a slightly decreased density in the CG compared to the FG region (see also [Appendix B](#)). The minimum-image setup suffers in principle from the same limitation, but the effective cutoff in the z -direction is 5 nm (compared to $R_c = 2.8$ nm for the spherical cutoff), which probably explains why the effect is negligible in this case. All these density artifacts (peaks at the interfaces and offsets) are essentially eliminated by applying a biasing potential, as can be seen from the blue curve in [Fig. 8\(a\)](#). As expected, the biasing potential in [Fig. 8\(b\)](#) reflects the main features of the unbiased density profile.

The corresponding curves for the argon-based ionic liquid are shown in [Figs. 8\(c\)](#) and [8\(d\)](#). Considering the high similarity of the results compared to the uncharged argon liquid, it appears that the presence or absence of small charges in the system does not have a significant influence on the density profiles.

V. CONCLUSIONS

The aim of this article was to introduce a new approach termed Adaptive Solvent-Scaling (AdSoS) for performing simulations of a solute embedded in a FG solvent region (for an accurate representation of the short-range solvation) itself surrounded by a CG solvent region (for an efficient representation of the long-range solvation) with a continuous FG \leftrightarrow CG switching of the solvent resolution across a buffer layer. This setup is very similar to the AdResS scheme. However, instead of interpolating between distinct FG and CG models, the AdSoS approach scales the dimensions of the FG solvent by a factor s , accompanied by an s -dependent modulation of the atomic masses and interaction parameters. In the case of homogeneous systems, this modulation is designed to achieve a perfect isomorphism between the dynamics of the FG model and that of the scaled CG model, irrespective of the s -value. Time, temperature, and energetic properties are not affected by the scaling. This is not the case for the pressure, which is reduced upon increasing s , accompanied by an increase in the compressibility. Most importantly, the scaling preserves the volumetric dispersive and dielectric solvation properties of the solvent relative to a FG solute.

In the context of AdSoS, the system involves interactions between solvent molecules at different local s -values, and an exact isomorphism to some reference system can no longer be defined. However, the method is still expected to benefit from a qualitative similarity with the homogeneous-scaling situation. The AdSoS setup is designed to keep the thermodynamic mismatches in the system to a minimum by imposing near-ideal mixing properties of scaled molecules at comparable s -values, a continuous change in s with position and appropriate pressure variations enabled by the drift force. However density artifacts may still occur. These effects are limited and can be corrected by application of a grid-based biasing potential. This potential should be calibrated in the absence of solute, i.e., in the situation where solvent homogeneity is expected, and is assumed portable from system to system, i.e., applicable irrespective of the solute. Note also that the time step appropriate for an accurate integration of the FG model is expected to produce a similarly accurate integration throughout the entire AdSoS system.

This article provided an initial application of AdSoS to atomic liquids with Lennard-Jones plus Coulomb interactions in a setup involving the pure liquid in slab geometry. Future developments will follow three main directions, as briefly discussed below.

First, a number of *ad hoc* choices involved in AdSoS may have a significant influence on its accuracy, and should thus be analyzed in more detail. These include in particular: (i) the functional form selected for the position dependence of the scaling factor s (e.g., piecewise linear as used here vs smoother curve choices; see [Appendix B](#)); (ii) the combination rule adopted to define the pairwise s -factor based on the s -factors of the interacting atoms (e.g., geometric mean as used here vs other combination rule); (iii) the appropriate choice of s_{\max} and the sizes of the FG, SG, and CG compartments (in relation to the solute size and properties, the requirement for sufficient FG solvation of this solute, and the requirement for a negligible contribution of the incorrectly scaling Lennard-Jones repulsive term); and (iv) the implementation of cutoff truncation for the non-bonded interactions (e.g., minimum-image or fixed spherical cutoff with reaction field vs s -dependent cutoff ranges). Concerning the last point, it may also be of interest to investigate the applicability of lattice-sum methods¹⁵² (Ewald¹⁵³ or particle-mesh^{154–157}) in AdSoS. These approaches would incorporate long-range effects (in an artificially periodic rather than mean-field fashion¹⁵⁸), while formally eliminating the dependence of the results on a truncation cutoff, the selection of which is ambiguous. However, the choice of a real-space cutoff and, for particle-mesh methods, of a reciprocal-space grid spacing leading to fast convergence would remain problematic (different requirements for the FG and CG regions).

Second, the scheme should be extended to more practically relevant situations. These include in particular: (i) molecular dipolar solvents (e.g., water); (ii) radial geometries (i.e., spherical layers for the FG, SG, and CG regions); and (iii) inclusion of a solute (e.g., membrane in the slab geometry and ion, dipole, or peptide in a radial geometry). These extensions have already been explored and will be reported in a forthcoming article. In the context of water, they involve the use of a per-molecule (rather than per-atom) scaling factor, the adjustment of the procedure to enforce s -dependent bond-length constraints, and the introduction of a second biasing potential correcting for small artifacts in the dipolar orientation.

In addition, two more challenging methodology developments should be tackled, namely: (i) how to generalize the approach to aqueous solutions at finite ionic strengths; and (ii) how to generalize the approach to simulations performed at constant pressure. The first issue is challenging considering that the interaction between FG solute charges and ionic charges in the CG region will scale with $s^{1/2}$, thereby altering the interactions of a solute with its counterion environment. The second issue is also non-trivial considering the inhomogeneity of the system pressure. Finally, it may be of interest to investigate the feasibility of flexible-boundary^{64,159} (rather than fixed-boundary) as well as distance-based^{160,161} (rather than position-based) variants of the scaling.

ACKNOWLEDGMENTS

Financial support from the Swiss National Science Foundation (Grant No. 200021-175944) is gratefully acknowledged.

APPENDIX A: DERIVATION OF EQS. (11) AND (12)

In this appendix, the expressions of Eqs. (11) and (12) for the three terms in Eq. (10) are derived explicitly in the context of an atomic liquid with Lennard-Jones plus Coulomb interactions. The derivations follow from the Hamiltonian expression of Eq. (7) with its two terms given by Eqs. (8) and (9), along with the scalings of Eq. (6).

For the first term of Eq. (10), one finds

$$\begin{aligned} \left(\frac{\partial \mathcal{H}}{\partial \mathbf{r}} \right)_{\mathbf{p}, s} \left(\frac{\partial \mathbf{r}}{\partial s} \right)_{\mathbf{r}^*} &= \left(6 \sum_i^N \sum_{j>i}^N \tilde{c}_{6,i} \tilde{c}_{6,j} \tilde{r}_{ij}^{-7} - 12 \sum_i^N \sum_{j>i}^N \tilde{c}_{12,i} \tilde{c}_{12,j} \tilde{r}_{ij}^{-13} \right. \\ &\quad \left. - \frac{1}{4\pi\epsilon_0} \sum_i^N \sum_{j>i}^N \tilde{q}_i \tilde{q}_j \tilde{r}_{ij}^{-2} \right) \frac{\tilde{\mathbf{r}}_{ij}}{\tilde{r}_{ij}} \cdot s^{-1} \tilde{\mathbf{r}}_{ij} \\ &= 2s^{-1} \mathcal{W}(\tilde{\mathbf{r}}, s), \end{aligned} \quad (\text{A1})$$

with the virial \mathcal{W} given by

$$\mathcal{W}(\mathbf{r}, s) = 3 \sum_i^N \sum_{j>i}^N \tilde{c}_{6,i} \tilde{c}_{6,j} \tilde{r}_{ij}^{-6} - 6 \sum_i^N \sum_{j>i}^N \tilde{c}_{12,i} \tilde{c}_{12,j} \tilde{r}_{ij}^{-12} - \frac{1}{8\pi\epsilon_0} \sum_i^N \sum_{j>i}^N \tilde{q}_i \tilde{q}_j \tilde{r}_{ij}^{-1}. \quad (\text{A2})$$

For the second term in Eq. (10), one finds

$$\left(\frac{\partial \mathcal{H}}{\partial \tilde{\mathbf{p}}} \right)_{\mathbf{r}, s} \left(\frac{\partial \tilde{\mathbf{p}}}{\partial s} \right)_{\mathbf{p}^*} = \sum_i^N \frac{2\tilde{\mathbf{p}}_i}{2\tilde{m}_i} \cdot (-s^{-1}\tilde{\mathbf{p}}_i) = -2s^{-1}\mathcal{K}(\tilde{\mathbf{p}}, s), \quad (\text{A3})$$

with the kinetic energy \mathcal{K} defined in Eq. (17). Finally, for the third term of Eq. (10), one finds

$$\begin{aligned} \left(\frac{\partial \mathcal{H}}{\partial s} \right)_{\tilde{\mathbf{r}}, \tilde{\mathbf{p}}} &= \sum_i^N \left(-\frac{\tilde{\mathbf{p}}_i^2}{2\tilde{m}_i^2} \right) (-2s^{-3}m_i^*) - 2 \sum_i^N \sum_{j>i}^N (\tilde{c}_{6,j} \tilde{r}_{ij}^{-6}) (3s^2 c_{6,i}^*) \\ &\quad + 2 \sum_i^N \sum_{j>i}^N (\tilde{c}_{12,j} \tilde{r}_{ij}^{-12}) (6s^5 c_{12,i}^*) \\ &\quad + \frac{2}{4\pi\epsilon_0} \sum_i^N \sum_{j>i}^N (\tilde{q}_j \tilde{r}_{ij}^{-1}) \left(\frac{1}{2}s^{-1/2} q_i^* \right) \\ &= s^{-1} [2\mathcal{K}(\tilde{\mathbf{p}}, s) - 2\mathcal{W}(\tilde{\mathbf{r}}, s)] = 3s^{-1} \tilde{V}(\tilde{\mathbf{r}}, \tilde{\mathbf{p}}, s), \end{aligned} \quad (\text{A4})$$

where the last equality follows from Eq. (13). As expected, the three terms cancel each other in the sum of Eq. (10). The third term accounts for the explicit s -dependence of the Hamiltonian and is the only one relevant in Eq. (19).

APPENDIX B: ALTERNATIVE $s(z)$ FUNCTIONS

Figure 9 investigates the effect of the cutoff, the time step, the width of the SG layer, and the choice of the scaling function $s(z)$ on the AdSoS density profiles. The magnitude of the density artifacts does not considerably change between the different $s(z)$ functions. In all cases, these artifacts are most pronounced in the regions of high curvature of the corresponding switching function. Even though the sine function⁶⁶ (and ONIOM-XS¹⁶²) cancels the first (and second) derivative(s) at the boundaries, the density artifacts are merely shifted toward the center of the SG regions.

The time step does not play a measurable role in the context of the piecewise-linear s -gradient, as can be seen in the upper row of Fig. 9(b). When switching from the minimum-image cutoff [Fig. 9(a)] to a spherical cutoff at 2.8 nm, the FG and CG densities are no longer aligned, as the dispersive interactions of the CG atoms are more affected by the truncation compared to those of the

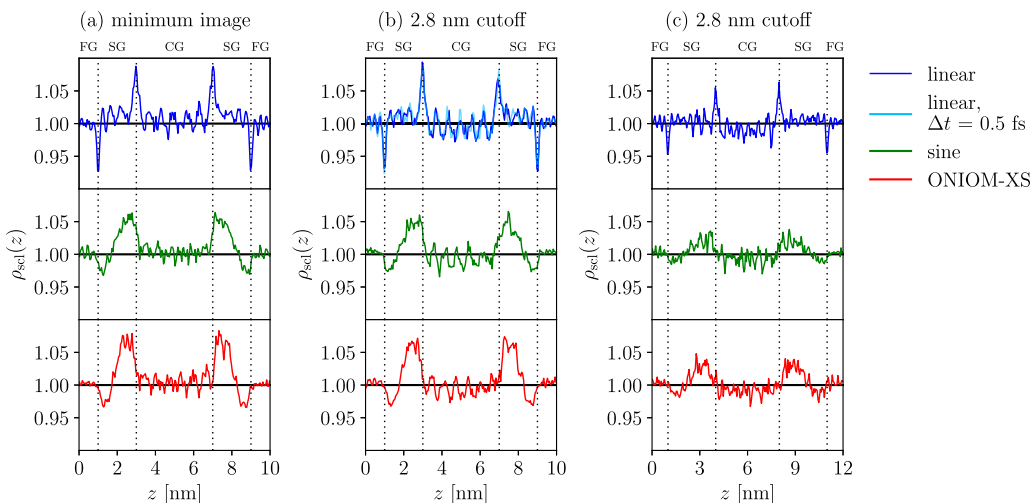


FIG. 9. Scaled density profiles for AdSoS simulations of liquid argon with $s_{\max} = 2$. Three different functions for $s(z)$ are compared: the piecewise-linear function of Eq. (39), a sine function⁶⁶ [see Eq. (1) therein], and the ONIOM-XS function.¹⁶² Unless otherwise indicated, the integration time step is 2 fs. The successive columns correspond to (a) results obtained with a minimum-image cutoff, or (b) and (c) interactions truncated at 2.8 nm. In (a) and (b), the boundary layer d_{SG} is set to 2 nm, whereas in (c), it is set to 3 nm.

FG atoms. The magnitude of the density artifacts significantly decreases upon broadening of the SG layer [Fig. 9(c)] due to the decrease in the magnitude of the *s*-gradient.

DATA AVAILABILITY

The data that support the findings of this study are available from the corresponding author upon reasonable request.

REFERENCES

- ¹C. J. Cramer and D. G. Truhlar, "Implicit solvation models: Equilibria, structure, spectra, and dynamics," *Chem. Rev.* **99**, 2161–2200 (1999).
- ²B. Roux and T. Simonson, "Implicit solvent models," *Biophys. Chem.* **78**, 1–20 (1999).
- ³M. Feig and C. L. Brooks III, "Recent advances in the development and application of implicit solvent models in biomolecule simulations," *Curr. Opin. Struct. Biol.* **14**, 217–224 (2004).
- ⁴J. Tomasi, B. Mennucci, and R. Cammi, "Quantum mechanical continuum solvation models," *Chem. Rev.* **105**, 2999–3093 (2005).
- ⁵A. Klamt, "The COSMO and COSMO-RS solvation models," *Wiley Interdiscip. Rev.: Comput. Mol. Sci.* **1**, 699–709 (2011).
- ⁶A. V. Onufriev and D. A. Case, "Generalized Born implicit solvent models for biomolecules," *Annu. Rev. Biophys.* **48**, 275–296 (2019).
- ⁷J. Baschnagel, K. Binder, P. Doruker, A. A. Gusev, O. Hahn, K. Kremer, W. L. Mattice, F. Müller-Plathe, M. Murat, W. Paul, S. Santos, U. W. Suter, and W. Tries, "Bridging the gap between atomistic and coarse-grained models of polymers: Status and perspectives," *Adv. Polym. Sci.* **152**, 41–156 (2000).
- ⁸F. Müller-Plathe, "Coarse-graining in polymer simulations: From the atomistic to the mesoscopic scale and back," *ChemPhysChem* **3**, 754–769 (2002).
- ⁹S. O. Nielsen, C. F. Lopez, G. Srinivas, and M. L. Klein, "Coarse grain models and the computer simulation of soft materials," *J. Phys.: Condens. Matter* **16**, R481–R512 (2004).
- ¹⁰S. J. Marrink, H. J. Risselada, S. Yefimov, D. P. Tieleman, and A. H. de Vries, "The MARTINI force field: Coarse grained model for biomolecular simulations," *J. Phys. Chem. B* **111**, 7812–7824 (2007).
- ¹¹S. C. L. Kamerlin, S. Vicatos, A. Dryga, and A. Warshel, "Coarse-grained (multiscale) simulations in studies of biophysical and chemical systems," *Annu. Rev. Phys. Chem.* **62**, 41–64 (2011).
- ¹²S. Riniker, J. R. Allison, and W. F. van Gunsteren, "On developing coarse-grained models for biomolecular simulation: A review," *Phys. Chem. Chem. Phys.* **14**, 12423–12430 (2012).
- ¹³M. G. Saunders and G. A. Voth, "Coarse-graining methods for computational biology," *Annu. Rev. Biophys.* **42**, 73–93 (2013).
- ¹⁴H. I. Ingólfsson, C. A. Lopez, J. J. Uusitalo, D. H. de Jong, S. M. Gopal, X. Periole, and S. J. Marrink, "The power of coarse graining in biomolecular simulations," *Wiley Interdiscip. Rev.: Comput. Mol. Sci.* **4**, 225–248 (2014).
- ¹⁵P. Kar and M. Feig, "Coarse-grained modeling of proteins," *Adv. Protein Chem. Struct. Biol.* **96**, 143–180 (2014).
- ¹⁶A. J. Pak and G. A. Voth, "Advances in coarse-grained modeling of macromolecular complexes," *Curr. Opin. Struct. Biol.* **52**, 119–126 (2018).
- ¹⁷T. E. Gartner III and A. Jayaraman, "Modeling and simulations of polymers: A roadmap," *Macromolecules* **52**, 755–786 (2019).
- ¹⁸N. Singh and W. Li, "Recent advances in coarse-grained models for biomolecules and their applications," *Int. J. Mol. Sci.* **20**, 3774 (2019).
- ¹⁹S. Y. Joshi and S. A. Deshmukh, "A review of advancements in coarse-grained molecular dynamics simulations," *Mol. Simul.* **47**, 786–803 (2021).
- ²⁰M. Levitt and S. Lifson, "Refinement of protein conformations using a macromolecular energy minimization procedure," *J. Mol. Biol.* **46**, 269–279 (1969).
- ²¹G. S. Ayton, W. G. Noid, and G. A. Voth, "Multiscale modeling of biomolecular systems: In serial and in parallel," *Curr. Opin. Struct. Biol.* **17**, 192–198 (2008).
- ²²S. O. Nielsen, R. E. Bulo, P. B. Moore, and B. Ensing, "Recent progress in adaptive multiscale molecular dynamics of soft matter," *Phys. Chem. Chem. Phys.* **12**, 12401–12414 (2010).
- ²³K. Meier, A. Choutko, J. Dolenc, A. P. Eichenberger, S. Riniker, and W. F. van Gunsteren, "Multi-resolution simulation of biomolecular systems: A review of methodological issues," *Angew. Chem., Int. Ed. Engl.* **52**, 2820–2834 (2013).
- ²⁴A. Kovalenko and S. Gusarov, "Multiscale methods framework: Self-consistent coupling of molecular theory of solvation with quantum chemistry, molecular simulations, and dissipative particle dynamics," *Phys. Chem. Chem. Phys.* **20**, 2947–2969 (2018).
- ²⁵H. V. Guzman, N. Tretyakov, H. Kobayashi, A. C. Fogarty, K. Kreis, J. Krajniak, C. Junghans, K. Kremer, and T. Stuehn, "ESPResSo++ 2.0: Advanced methods for multiscale molecular simulation," *Comput. Phys. Commun.* **238**, 66–76 (2019).
- ²⁶W. Tschöp, K. Kremer, O. Hahn, J. Batoulis, and T. Bürger, "Simulation of polymer melts. II. From coarse-grained models back to atomistic description," *Acta Polym.* **49**, 75–79 (1998).
- ²⁷B. Hess, S. León, N. van der Vegt, and K. Kremer, "Long time atomistic polymer trajectories from coarse grained simulations: Bisphenol-A polycarbonate," *Soft Matter* **2**, 409–414 (2006).
- ²⁸A. P. Heath, L. E. Kavraki, and C. Clementi, "From coarse-grain to all-atom: Toward multiscale analysis of protein landscapes," *Proteins* **68**, 646–661 (2007).
- ²⁹A. J. Rzepiela, L. V. Schäfer, N. Goga, H. J. Risselada, A. H. De Vries, and S. J. Marrink, "Reconstruction of atomistic details from coarse-grained structures," *J. Comput. Chem.* **31**, 1333–1343 (2010).
- ³⁰P. J. Stansfeld and M. S. P. Sansom, "From coarse grained to atomistic: A serial multiscale approach to membrane protein simulations," *J. Chem. Theory Comput.* **7**, 1157–1166 (2011).
- ³¹T. A. Wassenaar, K. Pluhackova, R. A. Böckmann, S. J. Marrink, and D. P. Tielemans, "Going backward: A flexible geometric approach to reverse transformation from coarse grained to atomistic models," *J. Chem. Theory Comput.* **10**, 676–690 (2014).
- ³²J. Krajniak, S. Pandiyan, E. Nies, and G. Samaey, "Generic adaptive resolution method for reverse mapping of polymers from coarse-grained to atomistic descriptions," *J. Chem. Theory Comput.* **12**, 5549–5562 (2016).
- ³³C. Nowak, M. Misra, and F. A. Escobedo, "Framework for inverse mapping chemistry-agnostic coarse-grained simulation models into chemistry-specific models," *J. Chem. Inf. Model.* **59**, 5045–5056 (2019).
- ³⁴Y. An and S. A. Deshmukh, "Machine learning approach for accurate backmapping of coarse-grained models to all-atom models," *Chem. Commun.* **56**, 9312–9315 (2019).
- ³⁵W. Li, C. Burkhardt, P. Polińska, V. Harmandaris, and M. Doxastakis, "Backmapping coarse-grained macromolecules: An efficient and versatile machine learning approach," *J. Chem. Phys.* **153**, 041101 (2020).
- ³⁶M. Li, B. Teng, W. Lu, and J. Z. Zhang, "Atomic-level reconstruction of biomolecules by a rigid-fragment- and local-frame-based (RF-LF) strategy," *J. Mol. Model.* **26**, 31 (2020).
- ³⁷T. Z. Lwin and R. Luo, "Overcoming entropic barrier with coupled sampling at dual resolutions," *J. Chem. Phys.* **123**, 194904 (2005).
- ³⁸M. Christen and W. F. van Gunsteren, "Multigraining: An algorithm for simultaneous fine-grained and coarse-grained simulation of molecular systems," *J. Chem. Phys.* **124**, 154106 (2006).
- ³⁹E. Lyman, F. M. Ytreberg, and D. M. Zuckerman, "Resolution exchange simulation," *Phys. Rev. Lett.* **96**, 028105 (2006).
- ⁴⁰E. Lyman and D. M. Zuckerman, "Resolution exchange simulation with incremental coarsening," *J. Chem. Theory Comput.* **2**, 656–666 (2006).
- ⁴¹P. Liu and G. A. Voth, "Smart resolution replica exchange: An efficient algorithm for exploring complex energy landscapes," *J. Chem. Phys.* **126**, 045106 (2007).
- ⁴²P. Liu, Q. Shi, E. Lyman, and G. A. Voth, "Reconstructing atomistic detail for coarse-grained models with resolution exchange," *J. Chem. Phys.* **129**, 114103 (2008).
- ⁴³Y. Yamamori and A. Kitao, "MuSTAR MD: Multi-scale sampling using temperature accelerated and replica exchange molecular dynamics," *J. Chem. Phys.* **139**, 145105 (2013).
- ⁴⁴K. H. Lee and J. Chen, "Multiscale enhanced sampling of intrinsically disordered protein conformations," *J. Comput. Chem.* **37**, 550–557 (2016).
- ⁴⁵Y. Lu, X. Zhou, and Z. OuYang, "Smoothing potential energy surface of proteins by hybrid coarse grained approach," *Chin. Phys. B* **26**, 050202 (2017).

- ⁴⁶Y. Liu, W. Pezeshkian, J. Barnoud, A. H. de Vries, and S. J. Marrink, "Coupling coarse-grained to fine-grained models via Hamiltonian replica exchange," *J. Chem. Theory Comput.* **16**, 5313–5322 (2020).
- ⁴⁷W. Li and S. Takada, "Self-learning multiscale simulation for achieving high accuracy and high efficiency simultaneously," *J. Chem. Phys.* **130**, 214108 (2009).
- ⁴⁸H. Shimoyama, Y. Yonezawa, and H. Nakamura, "Enhanced free-energy calculation using multiscale simulation," *J. Chem. Phys.* **133**, 135101 (2010).
- ⁴⁹A. Samiotakis, D. Homouz, and M. S. Cheung, "Multiscale investigation of chemical interference in proteins," *J. Chem. Phys.* **132**, 175101 (2010).
- ⁵⁰W. Li and S. Takada, "Characterizing protein energy landscape by self-learning multiscale simulations: Application to a designed β -hairpin," *Biophys. J.* **99**, 3029–3037 (2010).
- ⁵¹W. Li, H. Yoshii, N. Hori, T. Kameda, and S. Takada, "Multiscale methods for protein folding simulations," *Methods* **52**, 106–114 (2010).
- ⁵²Y. Chen and B. Roux, "Enhanced sampling of an atomic model with hybrid nonequilibrium molecular dynamics—Monte Carlo simulations guided by a coarse-grained model," *J. Chem. Theory Comput.* **11**, 3572–3583 (2015).
- ⁵³S. Hunkler, T. Lemke, C. Peter, and O. Kukharenko, "Back-mapping based sampling: Coarse grained free energy landscapes as a guideline for atomistic exploration," *J. Chem. Phys.* **151**, 154102 (2019).
- ⁵⁴K. Wu, S. Xu, B. Wan, P. Xiu, and X. Zhou, "A novel multiscale scheme to accelerate atomistic simulations of bio-macromolecules by adaptively driving coarse-grained coordinates," *J. Chem. Phys.* **152**, 114115 (2020).
- ⁵⁵C. F. Abrams, "Concurrent dual-resolution Monte Carlo simulation of liquid methane," *J. Chem. Phys.* **123**, 234101 (2005).
- ⁵⁶M. Neri, C. Anselmi, M. Cascella, A. Maritan, and P. Carloni, "Coarse-grained model of proteins incorporating atomistic detail of the active site," *Phys. Rev. Lett.* **95**, 218102 (2005).
- ⁵⁷A. J. Rzepiela, M. Louhivuori, C. Peter, and S. J. Marrink, "Hybrid simulations: Combining atomistic and coarse-grained force fields using virtual sites," *Phys. Chem. Chem. Phys.* **13**, 10437–10448 (2011).
- ⁵⁸Y. Liu, A. H. De Vries, J. Barnoud, W. Pezeshkian, J. Melcr, and S. J. Marrink, "Dual resolution membrane simulations using virtual sites," *J. Phys. Chem. B* **124**, 3944–3953 (2020).
- ⁵⁹S. Riniker, A. P. Eichenberger, and W. F. van Gunsteren, "Structural effects of an atomic-level layer of water molecules around proteins solvated in supra-molecular coarse-grained water," *J. Phys. Chem. B* **116**, 8873–8879 (2012).
- ⁶⁰Z. Lin and W. F. van Gunsteren, "Free enthalpy differences between α -, π -, and 3_{10} -helices of an atomic level fine-grained alanine deca-peptide solvated in supramolecular coarse-grained water," *J. Chem. Theory Comput.* **9**, 1328–1333 (2013).
- ⁶¹P. Sokkar, S. M. Choi, and Y. M. Rhee, "Simple method for simulating the mixtures of atomistic and coarse-grained molecular systems," *J. Chem. Theory Comput.* **9**, 3728–3739 (2013).
- ⁶²H. C. Gonzalez, L. Darré, and S. Pantano, "Transferable mixing of atomistic and coarse-grained water models," *J. Phys. Chem. B* **117**, 14438–14448 (2013).
- ⁶³A. B. Kuhn, S. M. Gopal, and L. V. Schäfer, "On using atomistic solvent layers in hybrid all-atom/coarse-grained molecular dynamics simulations," *J. Chem. Theory Comput.* **11**, 4460–4472 (2015).
- ⁶⁴O. M. Szklarczyk, N. S. Bieler, P. H. Hünenberger, and W. F. van Gunsteren, "Flexible boundaries for multiresolution solvation: An algorithm for spatial multiscaling in molecular dynamics simulations," *J. Chem. Theory Comput.* **11**, 5447–5463 (2015).
- ⁶⁵A. Renevey and S. Riniker, "Benchmarking hybrid atomistic/coarse-grained schemes for proteins with an atomistic water layer," *J. Phys. Chem. B* **123**, 3033–3042 (2019).
- ⁶⁶H. Wang and A. Agarwal, "Adaptive resolution simulation in equilibrium and beyond," *Eur. Phys. J.: Spec. Top.* **224**, 2269–2287 (2015).
- ⁶⁷A. W. Duster, C. H. Wang, C. M. Garza, D. E. Miller, and H. Lin, "Adaptive quantum/molecular mechanics: What have we learned, where are we, and where do we go from here?," *Wiley Interdiscip. Rev.: Comput. Mol. Sci.* **7**, e1310 (2017).
- ⁶⁸L. D. Site and M. Praprotnik, "Molecular systems with open boundaries: Theory and simulation," *Phys. Rep.* **693**, 1–56 (2017).
- ⁶⁹J. Zavadlav, S. Bevc, and M. Praprotnik, "Adaptive resolution simulations of biomolecular systems," *Eur. Biophys. J.* **46**, 821–835 (2017).
- ⁷⁰J. Zavadlav, M. N. Melo, S. J. Marrink, and M. Praprotnik, "Adaptive resolution simulation of an atomistic protein in MARTINI water," *J. Chem. Phys.* **140**, 054114 (2014).
- ⁷¹Z. Wu, Q. Cui, and A. Yethiraj, "Driving force for the association of hydrophobic peptides: The importance of electrostatic interactions in coarse-grained water models," *J. Phys. Chem. Lett.* **2**, 1794–1798 (2011).
- ⁷²S. Riniker, A. P. Eichenberger, and W. F. van Gunsteren, "Solvating atomic level fine-grained proteins in supra-molecular level coarse-grained water for molecular dynamics simulations," *Eur. Biophys. J.* **41**, 647–661 (2012).
- ⁷³X. Liu, C. Wang, J. Wang, Z. Li, H. Zhao, and R. Luo, "Exploring charge-central strategy in the solution of Poisson's equation for biomolecular applications," *Phys. Chem. Chem. Phys.* **15**, 129–141 (2013).
- ⁷⁴W. Han and K. Schulten, "Further optimization of a hybrid united-atom and coarse-grained force field for folding simulations: Improved backbone hydration and interactions between charged side chains," *J. Chem. Theory Comput.* **8**, 4413–4424 (2012).
- ⁷⁵M. Orsi, W. Ding, and M. Palaiokostas, "Direct mixing of atomistic solutes and coarse-grained water," *J. Chem. Theory Comput.* **10**, 4684–4693 (2014).
- ⁷⁶W. Huang, S. Riniker, and W. F. van Gunsteren, "Rapid sampling of folding equilibria of β -peptides in methanol using a supramolecular solvent model," *J. Chem. Theory Comput.* **10**, 2213–2223 (2014).
- ⁷⁷W. Huang, N. Hansen, and W. F. van Gunsteren, "On the use of a supramolecular coarse-grained model for the solvent in simulations of the folding equilibrium of an octa- β -peptide in MeOH and H₂O," *Helv. Chim. Acta* **97**, 1591–1605 (2014).
- ⁷⁸S. Genheden and J. W. Essex, "A simple and transferable all-atom/coarse-grained hybrid model to study membrane processes," *J. Chem. Theory Comput.* **11**, 4749–4759 (2015).
- ⁷⁹S. Genheden, "Predicting partition coefficients with a simple all-atom/coarse-grained hybrid model," *J. Chem. Theory Comput.* **12**, 297–304 (2016).
- ⁸⁰X. C. Yan, J. Tirado-Rives, and W. L. Jorgensen, "Hydration properties and solvent effects for all-atom solutes in polarizable coarse-grained water," *J. Phys. Chem. B* **120**, 8102–8114 (2016).
- ⁸¹A. Renevey and S. Riniker, "Improved accuracy of hybrid atomistic/coarse-grained simulations using reparametrised interactions," *J. Chem. Phys.* **146**, 124131 (2017).
- ⁸²J. Zavadlav, M. N. Melo, A. V. Cunha, A. H. de Vries, S. J. Marrink, and M. Praprotnik, "Adaptive resolution simulation of MARTINI solvents," *J. Chem. Theory Comput.* **10**, 2591–2598 (2014).
- ⁸³J. Zavadlav, S. J. Marrink, and M. Praprotnik, "Adaptive resolution simulation of supramolecular water: The concurrent making, breaking, and remaking of water bundles," *J. Chem. Theory Comput.* **12**, 4138–4145 (2016).
- ⁸⁴J. Zavadlav, S. J. Marrink, and M. Praprotnik, "Multiscale simulation of protein hydration using the SWINGER dynamical clustering algorithm," *J. Chem. Theory Comput.* **14**, 1754–1761 (2018).
- ⁸⁵J. Zavadlav, S. J. Marrink, and M. Praprotnik, "SWINGER: A clustering algorithm for concurrent coupling of atomistic and supramolecular liquids," *Interface Focus* **9**, 20180075 (2019).
- ⁸⁶M. Praprotnik, L. D. Site, and K. Kremer, "Adaptive resolution molecular-dynamics simulation: Changing the degrees of freedom on the fly," *J. Chem. Phys.* **123**, 224106 (2005).
- ⁸⁷M. Praprotnik, L. D. Site, and K. Kremer, "Multiscale simulation of soft matter: From scale bridging to adaptive resolution," *Annu. Rev. Phys. Chem.* **59**, 545–571 (2008).
- ⁸⁸S. Poblete, M. Praprotnik, K. Kremer, and L. D. Site, "Coupling different level of resolution in molecular simulations," *J. Chem. Phys.* **132**, 114101 (2010).
- ⁸⁹M. Praprotnik, S. Poblete, and K. Kremer, "Statistical physics problems in adaptive resolution computer simulations of complex fluids," *J. Stat. Phys.* **145**, 946–966 (2011).
- ⁹⁰S. Fritsch, S. Poblete, C. Junghans, G. Cicotti, L. D. Site, and K. Kremer, "Adaptive resolution molecular dynamics simulation through coupling to an internal particle reservoir," *Phys. Rev. Lett.* **108**, 170602 (2012).
- ⁹¹R. Potestio, S. Fritsch, P. Español, R. Delgado-Buscalioni, K. Kremer, R. Everaers, and D. Donadio, "Hamiltonian adaptive resolution simulation for molecular liquids," *Phys. Rev. Lett.* **110**, 108301 (2013).

- ⁹²R. Potestio, P. Espanol, R. Delgado-Buscallioni, R. Everaers, K. Kremer, and D. Donadio, “Monte Carlo adaptive resolution simulation of multicomponent molecular liquids,” *Phys. Rev. Lett.* **111**, 060601 (2013).
- ⁹³A. Agarwal, H. Wang, C. Schütte, and L. D. Site, “Chemical potential of liquids and mixtures via adaptive resolution simulation,” *J. Chem. Phys.* **141**, 034102 (2014).
- ⁹⁴P. Españo, R. Delgado-Buscallioni, R. Everaers, R. Potestio, D. Donadio, and K. Kremer, “Statistical mechanics of Hamiltonian adaptive resolution simulations,” *J. Chem. Phys.* **142**, 064115 (2015).
- ⁹⁵B. Ensing, S. O. Nielsen, P. B. Moore, M. L. Klein, and M. Parrinello, “Energy conservation in adaptive hybrid atomistic/coarse-grain molecular dynamics,” *J. Chem. Theory Comput.* **3**, 1100–1105 (2007).
- ⁹⁶A. Heyden and D. G. Truhlar, “Conservative algorithm for an adaptive change of resolution in mixed atomistic/coarse-grained multiscale simulations,” *J. Chem. Theory Comput.* **4**, 217–221 (2008).
- ⁹⁷J. A. Wagoner and V. S. Pande, “A smoothly decoupled particle interface: New methods for coupling explicit and implicit solvent,” *J. Chem. Phys.* **134**, 214103 (2011).
- ⁹⁸J. A. Wagoner and V. S. Pande, “Finite domain simulations with adaptive boundaries: Accurate potentials and nonequilibrium movesets,” *J. Chem. Phys.* **139**, 234114 (2013).
- ⁹⁹S. Artemova and S. Redon, “Adaptively restrained particle simulations,” *Phys. Rev. Lett.* **109**, 190201 (2012).
- ¹⁰⁰M. G. Guenza, “Advancements in multi scale modeling: Adaptive resolution simulations and related issues,” *Eur. Phys. J.: Spec. Top.* **224**, 2491–2495 (2015).
- ¹⁰¹R. Delgado-Buscallioni, “Thermodynamics of adaptive molecular resolution,” *Philos. Trans. R. Soc., A* **374**, 20160152 (2016).
- ¹⁰²R. Fiorentini, K. Kremer, R. Potestio, and A. C. Fogarty, “Using force-based adaptive resolution simulations to calculate solvation free energies of amino acid sidechain analogues,” *J. Chem. Phys.* **146**, 244113 (2017).
- ¹⁰³S. O. Nielsen, P. B. Moore, and B. Ensing, “Adaptive multiscale molecular dynamics of macromolecular fluids,” *Phys. Rev. Lett.* **105**, 237802 (2010).
- ¹⁰⁴T. Ichijo and M.-L. Tan, “Soft sticky dipole-quadrupole-octupole potential energy function for liquid water: An approximate expansion,” *J. Phys. Chem.* **124**, 134504 (2006).
- ¹⁰⁵P. A. Golubkov, J. C. Wu, and P. Ren, “A transferable coarse-grained model for hydrogen-bonding liquids,” *Phys. Chem. Chem. Phys.* **10**, 2050–2057 (2008).
- ¹⁰⁶V. Molinero and E. B. Moore, “Water modeled as an intermediate element between carbon and silicon,” *J. Phys. Chem. B* **113**, 4008–4016 (2009).
- ¹⁰⁷K. R. Hadley and C. McCabe, “On the investigation of coarse-grained models for water: Balancing computational efficiency and the retention of structural properties,” *J. Phys. Chem. B* **114**, 4590–4599 (2010).
- ¹⁰⁸S. O. Yesylevskyy, L. V. Schäfer, D. Sengupta, and S. J. Marrink, “Polarizable water model for the coarse-grained MARTINI force field,” *PLoS Comput. Biol.* **6**, e1000810 (2010).
- ¹⁰⁹Z. Wu, Q. Cui, and A. Yethiraj, “A new coarse-grained model for water: The importance of electrostatic interactions,” *J. Phys. Chem. B* **114**, 10524–10529 (2010).
- ¹¹⁰S. Riniker and W. F. van Gunsteren, “A simple, efficient polarisable coarse-grained water model for molecular dynamics simulations,” *J. Chem. Phys.* **134**, 084110 (2011).
- ¹¹¹K. R. Hadley and C. McCabe, “Coarse-grained molecular models of water: A review,” *Mol. Simul.* **38**, 671–681 (2012).
- ¹¹²M. Orsi, “Comparative assessment of the ELBA coarse-grained model for water,” *Mol. Phys.* **112**, 1566–1576 (2014).
- ¹¹³R. Qi, L.-P. Wang, Q. Wang, V. S. Pande, and P. Ren, “United polarizable multipole water model for molecular mechanics simulation,” *J. Chem. Phys.* **143**, 014504 (2015).
- ¹¹⁴M. Deng and H. Shen, “Coarse-grained model for water involving a virtual site,” *J. Phys. Chem. B* **120**, 733–739 (2016).
- ¹¹⁵K. K. Bejagam, S. Singh, Y. An, C. Berry, and S. A. Deshmukh, “PSO-assisted development of new transferable coarse-grained water models,” *J. Phys. Chem. B* **122**, 1958–1971 (2018).
- ¹¹⁶P. G. Lafond and S. Izvekov, “Multiscale coarse-graining with effective polarizabilities: A fully bottom-up approach,” *J. Chem. Theory Comput.* **14**, 1873–1886 (2018).
- ¹¹⁷S. Riniker, B. A. C. Horta, B. Thijssen, S. Gupta, W. F. van Gunsteren, and P. H. Hünenberger, “Temperature dependence of the dielectric permittivity of acetic acid, propionic acid and their methyl esters: A molecular dynamics simulation study,” *ChemPhysChem* **13**, 1182–1190 (2012).
- ¹¹⁸M. Fuhrmans, B. P. Sanders, S.-J. Marrink, and A. H. de Vries, “Effects of bundling on the properties of the SPC water model,” *Theor. Chem. Acc.* **125**, 335–344 (2010).
- ¹¹⁹S. M. Gopal, A. B. Kuhn, and L. V. Schäfer, “Systematic evaluation of bundled SPC water for biomolecular simulations,” *Phys. Chem. Chem. Phys.* **17**, 8393–8406 (2015).
- ¹²⁰C. Krekeler, A. Agarwal, C. Junghans, M. Praprotnik, and L. D. Site, “Adaptive resolution molecular dynamics technique: Down to the essential,” *J. Chem. Phys.* **149**, 024104 (2018).
- ¹²¹S. Thaler, M. Praprotnik, and J. Zavadlav, “Back-mapping augmented adaptive resolution simulation,” *J. Chem. Phys.* **153**, 164118 (2020).
- ¹²²P. Depa, C. Chen, and J. K. Maranas, “Why are coarse-grained force fields too fast? A look at dynamics of four coarse-grained polymers,” *J. Chem. Phys.* **134**, 014903 (2011).
- ¹²³M. K. Meinel and F. Müller-Plathe, “Loss of molecular roughness upon coarse-graining predicts the artificially accelerated mobility of coarse-grained molecular simulation models,” *J. Chem. Theory Comput.* **16**, 1411–1419 (2020).
- ¹²⁴G. G. Rondina, M. C. Böhm, and F. Müller-Plathe, “Predicting the mobility increase of coarse-grained polymer models from excess entropy differences,” *J. Chem. Theory Comput.* **16**, 1431–1447 (2020).
- ¹²⁵M. Praprotnik, K. Kremer, and L. D. Site, “Adaptive molecular resolution via a continuous change of the phase space dimensionality,” *Phys. Rev. E* **75**, 017701 (2007).
- ¹²⁶M. Praprotnik, K. Kremer, and L. D. Site, “Fractional dimensions of phase space variables: A tool for varying the degrees of freedom of a system in a multiscale treatment,” *J. Phys. A: Math. Theor.* **40**, F281–F288 (2007).
- ¹²⁷J. E. Lennard-Jones, “The equation of state of gases and critical phenomena,” *Physica* **4**, 941–956 (1937).
- ¹²⁸C. A. Coulomb, “Sur l’électricité et le magnétisme, premier mémoire, construction et usage d’une balance électrique, fondée sur la propriété qu’ont les fils de métal, d’avoir une force de réaction de torsion proportionnelle à l’angle de torsion,” *Mem. Acad. R. Sci.* **1785**, 569–577 (1788).
- ¹²⁹R. J. Good and C. J. Hope, “New combining rule for intermolecular distances in intermolecular potential functions,” *J. Chem. Phys.* **53**, 540–543 (1970).
- ¹³⁰R. J. Good and C. J. Hope, “Test of combining rules for intermolecular distances—Potential function constants from second virial coefficients,” *J. Chem. Phys.* **55**, 111–116 (1971).
- ¹³¹P. H. Hünenberger, “Calculation of the group-based pressure in molecular simulations. I. A general formulation including Ewald and particle-particle-particle-mesh electrostatics,” *J. Chem. Phys.* **116**, 6880–6897 (2002).
- ¹³²K. Kreis and R. Potestio, “The relative entropy is fundamental to adaptive resolution simulations,” *J. Chem. Phys.* **145**, 044104 (2016).
- ¹³³K. Kreis, D. Donadio, K. Kremer, and R. Potestio, “A unified framework for force-based and energy-based adaptive resolution simulations,” *Europhys. Lett.* **108**, 30007 (2014).
- ¹³⁴H. S. Hansen and P. H. Hünenberger, “Using the local elevation method to construct optimized umbrella sampling potentials: Calculation of the relative free energies and interconversion barriers of glucopyranose ring conformers in water,” *J. Comput. Chem.* **31**, 1–23 (2010).
- ¹³⁵T. Huber, A. E. Torda, and W. F. van Gunsteren, “Local elevation: A method for improving the searching properties of molecular dynamics simulation,” *J. Comput.-Aided Mol. Des.* **8**, 695–708 (1994).
- ¹³⁶J. P. Valleau and G. M. Torrie, “A guide to Monte Carlo for statistical mechanics: I. Highways,” in *Modern Theoretical Chemistry*, edited by B. J. Berne (Plenum Press, New York, 1977), Vol. 5.
- ¹³⁷R. W. Hockney, “The potential calculation and some applications,” *Methods Comput. Phys.* **9**, 135–211 (1970).

- ¹³⁸R. Potestio, "Computer simulation of particles with position-dependent mass," *Eur. Phys. J. B* **87**, 245 (2014).
- ¹³⁹J. M. Sanz-Serna, "Symplectic integrators for Hamiltonian problems: An overview," *Acta Numerica* **1**, 243–286 (1991).
- ¹⁴⁰X. Dai, C. Le Bris, F. Legoll, and Y. Maday, "Symmetric parareal algorithms for Hamiltonian systems," *ESAIM: Math. Modell. Numer. Anal.* **47**, 717–742 (2013).
- ¹⁴¹M. Tao, "Explicit symplectic approximation of nonseparable Hamiltonians: Algorithm and long time performance," *Phys. Rev. E* **94**, 043303 (2016).
- ¹⁴²H. J. C. Berendsen, J. P. M. Postma, W. F. van Gunsteren, A. di Nola, and J. R. Haak, "Molecular dynamics with coupling to an external bath," *J. Chem. Phys.* **81**, 3684–3690 (1984).
- ¹⁴³M. P. Oliveira, M. Andrey, S. R. Rieder, L. Kern, D. F. Hahn, S. Riniker, B. A. C. Horta, and P. H. Hünenberger, "Systematic optimization of a fragment-based force-field based on experimental pure-liquid properties considering large compound families: Application to the saturated haloalkanes," *J. Chem. Theory Comput.* **16**, 7525–7555 (2020).
- ¹⁴⁴N. Schmid, A. P. Eichenberger, A. Choutko, S. Riniker, M. Winger, A. E. Mark, and W. F. van Gunsteren, "Definition and testing of the GROMOS force-field versions 54A7 and 54B7," *Eur. Biophys. J.* **40**, 843–856 (2011).
- ¹⁴⁵L. V. Woodcock, "Isothermal molecular dynamics calculations for liquid salts," *Chem. Phys. Lett.* **10**, 257–261 (1971).
- ¹⁴⁶W. G. Hoover, A. J. C. Ladd, and B. Moran, "High-strain-rate plastic flow studied via nonequilibrium molecular dynamics," *Phys. Rev. Lett.* **48**, 1818–1820 (1982).
- ¹⁴⁷D. J. Evans, "Computer 'experiment' for nonlinear thermodynamics of Couette flow," *J. Chem. Phys.* **78**, 3297–3302 (1983).
- ¹⁴⁸M. P. Allen and D. J. Tildesley, *Computer Simulation of Liquids* (Oxford University Press, New York, 1987).
- ¹⁴⁹J. A. Barker and R. O. Watts, "Monte Carlo studies of the dielectric properties of water-like models," *Mol. Phys.* **26**, 789–792 (1973).
- ¹⁵⁰I. G. Tironi, R. Sperb, P. E. Smith, and W. F. van Gunsteren, "A generalized reaction field method for molecular dynamics simulations," *J. Chem. Phys.* **102**, 5451–5459 (1995).
- ¹⁵¹H. S. Hansen, X. Daura, and P. H. Hünenberger, "Enhanced conformational sampling in molecular dynamics simulations of solvated peptides: Fragment-based local elevation umbrella sampling," *J. Chem. Theory Comput.* **6**, 2598–2621 (2010).
- ¹⁵²P. H. Hünenberger, "Lattice-sum methods for computing electrostatic interactions in molecular simulations," in *Simulation and Theory of Electrostatic Interactions in Solution: Computational Chemistry, Biophysics, and Aqueous Solution*, edited by G. Hummer and L. R. Pratt (American Institute of Physics, New York, 1999), Vol. 492.
- ¹⁵³P. P. Ewald, "Die berechnung optischer und elektrostatischer gitterpotentiale," *Ann. Phys.* **369**, 253–287 (1921).
- ¹⁵⁴R. W. Hockney and J. W. Eastwood, *Computer Simulation Using Particles* (McGraw-Hill, New York, 1981).
- ¹⁵⁵R. W. Hockney and J. W. Eastwood, *Computer Simulation Using Particles*, 2nd ed. (Institute of Physics Publishing, Bristol, UK, 1988).
- ¹⁵⁶T. Darden, D. York, and L. Pedersen, "Particle mesh Ewald: An $N - \log(N)$ method for Ewald sums in large systems," *J. Chem. Phys.* **98**, 10089–10092 (1993).
- ¹⁵⁷U. Essmann, L. Perera, M. L. Berkowitz, T. Darden, H. Lee, and L. G. Pedersen, "A smooth particle mesh Ewald method," *J. Chem. Phys.* **103**, 8577–8593 (1995).
- ¹⁵⁸A. Kubincová, S. Riniker, and P. H. Hünenberger, "Reaction-field electrostatics in molecular dynamics simulations: Development of a conservative scheme compatible with an atomic cutoff," *Phys. Chem. Chem. Phys.* **22**, 26419–26437 (2020).
- ¹⁵⁹K. Kreis, R. Potestio, K. Kremer, and A. C. Fogarty, "Adaptive resolution simulations with self-adjusting high-resolution regions," *J. Chem. Theory Comput.* **12**, 4067–4081 (2016).
- ¹⁶⁰S. Izvekov and G. A. Voth, "Mixed resolution modeling of interactions in condensed-phase systems," *J. Chem. Theory Comput.* **5**, 3232–3244 (2009).
- ¹⁶¹L. Shen and H. Hu, "Resolution-adapted all-atomic and coarse-grained model for biomolecular simulations," *J. Chem. Theory Comput.* **10**, 2528–2536 (2014).
- ¹⁶²T. Kerdcharoen and K. Morokuma, "ONIOM-XS: An extension of the ONIOM method for molecular simulation in condensed phase," *Chem. Phys. Lett.* **355**, 257–262 (2002).